TRIBHUVAN UNIVERSITY

INSTITUTE OF ENGINEERING

PASCHIMANCHAL CAMPUS

DESIGN AND FABRICATION OF A PESTICIDE SPRAYING DRONE IN NEPAL

by

Aakash Rai (PAS078BME001)

Sandesh Ghorsai (PAS078BME034)

Subash Mahara (PAS078BME043)

Sundar Chapagain (PAS078BME044)

Swabhiman Thapa (PAS078BME046)

A PROJECT REPORT

SUBMITTED TO THE DEPARTMENT OF MECHANICAL AND AUTOMOBILE ENGINEERING IN PARTIAL FULFILLMENT OF THE REQUIREMENTS FOR THE DEGREE OF BACHELOR IN MECHANICAL ENGINEERING

DEPARTMENT OF MECHANICAL AND AUTOMOBILE ENGINEERING

IOE, PASCHIMANCHAL CAMPUS

MARCH, 2026

COPYRIGHT

Head

Department of Automobile and Mechanical Engineering

Pashchimanchal Campus, Institute of Engineering

Pokhara-16, Nepal

TRIBHUVAN UNIVERSITY

INSTITUTE OF ENGINEERING

PASHCHIMANCHAL CAMPUS

DEPARTMENT OF MECHANICAL AND AUTOMOBILE ENGINEERING

The undersigned certify that they have read, and recommended to the Institute of Engineering for acceptance, a project report entitled "Design and Fabrication of a Pesticide Spraying Drone in Nepal" submitted by Aakash Rai, Sandesh Ghorsai, Subash Mahara, Sundar Chapagain and Swabhiman Thapa in partial fulfillment of the requirements for the degree of Bachelor in Mechanical Engineering.

Supervisor,
Dr. Prabij Joshi
Assistant Professor
Department of Mechanical and Automobile Engineering

External Examiner,
Dr. Durga Bastakoti
Assistant Professor
Department of Mechanical and Aerospace Engineering
Pulchowk Campus, Institute of Engineering, Tribhuvan University

----
Committee Chairperson,
Kiran Giri
Deputy Head
Department of Mechanical and Automobile Engineering

Date

ABSTRACT

The trend of UAVs in precision agriculture, crop monitoring and cost reduction has gained significance globally. Adaptation to drone technology is crucial for Nepal as 67% of the total population depends on agriculture according to the census of 2078. The project titled "Design and Fabrication of a Pesticide Spraying Drone in Nepal" is focused on designing a 0.5L pesticide carrying capacity drone and to study the possibilities of harnessing this technology within the country targeting smallholder farmers. Locally available materials meeting the design criteria were prioritized to fabricate the drone. A 3D model of the drone was modeled on SolidWorks and analyzed on ANSYS for stress and thrust parameters. A practical thrust-to-weight ratio of 1.6 was achieved with a payload of 4.9kg and flight time of five minutes. The deviation of simulated thrust of the propeller from practical thrust generated was 4.32%. The sprayer system consists of two adjustable cone-type nozzles, each with a diameter of 1.8mm, fed with a 12V diaphragm pump. The flight test data represents a sound performance of the drone with a payload of 200ml liquid with a maximum vibration level of 13 m/s^2 along the body z-axis. The spray uniformity was achieved at a flight altitude of 1400-1600mm above the spraying surface, concluding it an ideal spray height for this pesticide-spraying hexacopter. The calculated spray liquid loss was 25% and the measured average area of droplets was 9.035mm^2 from five different samples.

Keywords: Finite Element Analysis (FEA), Hexa-copter, Pesticide Spraying, SolidWorks, Precision Agriculture

ACKNOWLEDGEMENT

We want to express our gratitude to the Department of Mechanical and Automobile Engineering, IOE, Pashchimanchal Campus, for providing the opportunity and facilitating the necessary material and equipment during the development and fabrication of our project.

We would like to express our deepest appreciation to our project supervisor, **Asst. Prof. Prabij Joshi** for his invaluable support, guidance, regular supervision, and enormous counseling. We were able to develop new and innovative ideas due to your continuous encouragement and help.

We are thankful to the Deputy Head of the Department of Mechanical and Automobile Engineering, Pashchimanchal Campus, **Asst. Prof. Kiran Giri** for providing us with all the necessary facilities and academic support during the progression of the project.

We are extremely grateful to our family for their constant moral and financial support throughout the project duration and academic life.

We are thankful to all the people who helped us to complete our project directly and indirectly by providing raw materials, valuable information, and unforgettable encouragement.

April, 2026	Aakash Rai (PAS078BME001)
Pashchimanchal Campus	Sandesh Ghorsai (PAS078BME034)
Institute of Engineering (IOE)	Subash Mahara (PAS078BME043)
Tribhuvan University	Sundar Chapagain(PAS078BME044)
Pokhara	Swabhiman Thapa(PAS078BME046)

TABLE OF CONTENTS

LIST OF FIGURES

LIST OF TABLES

LIST OF ABBREVIATIONS

ABS	Acrylonitrile Butadiene Styrene
ACP	Aluminum Composite Panel
AFHDS	Automatic Frequency Hopping Digital System
ANSYS	Analysis System
BEC	Battery Elimination Circuit
BEMT	Blade Element Momentum Theory
BET	Blade Element Theory
BLDC	Brushless Direct Current
CAD	Computer Aided Design
CFD	Computational Fluid Dynamics
CNC	Computer Numerical Control
dBm	Decibel-milliwatts
DMS	Digital Spectrum Modulation
ESC	Electronic Speed Controller
FDM	Fused Diffusion Modelling
FEA	Finite Element Analysis
FEM	Finite Element Method
FMUv2	Flight Management Unit Version 2
GFSK	Gaussian Frequency Shift Keying
GPS	Global Positioning System
HA	Hector
IBUS	Intelligent Binary Unit System
IMU	Inertial Measurement Unit

Kgf	Kilogram Force
Kv	Kilo-volt
MRF	Multiple Reference Frame
NMD	Number Mean Diameter
PDB	Power Distribution Board
PID	Proportional Integral Derivative
PLA	Polylactic Acid
PPM	Pulse Position Modulation
PRESTO	Pressure Staggering Option
PTW	Payload Takeoff Weight
PVC	Polyvinyl Chloride
PWM	Pulse Width Modulation
RANS	Reynolds-Averaged Navier-Stokes
RTOS	Real Time Operating System
Rx	Receiver
SPI	Serial Peripheral Interface
SRAM	Static Random Access Memory
SST	Shear Stress Transport
STM32	STMicroelectronics 32–bit
Tx	Transmitter
UASS	Unmanned Aerial Spray System
UAV	Un-manned Air Vehicle
VDC	Volts Direct Current
VMD	Volume Mean Diameter

CHAPTER 1: INTRODUCTION

1.1 Background

Nepali farmers massively rely on agricultural activities to earn a livelihood and to generate an income with around 65% of the total population (World Bank, 2023) engaged on agricultural sector. Despite this huge number of people depending on agricultural sector, only 25.16% of the nation's GDP (*Nepal Rastra Bank Current Macroeconomic and Financial Situation of Nepal*, 2025) is contributed by agriculture, forestry and fishing. Small and fragmented landholding, low productivity and limited access to modern tools and technology for mechanization of agriculture in Nepal hinder peculiar growth in the nation’s GDP.

Over the years, the Government of Nepal has formulated several plans, policies and programs to foster agricultural economy, yet the outcomes of agricultural modernization, food security and financial security for farmers has not changed (Shahi, 2022). Nepal has varied geography and climate posing significant potential for fruit, crop and vegetable cultivation. Despite this huge potential of agricultural land and climatic condition, Nepal faces several challenges viz. limited access to modern farming technologies, fragmented landholdings, varied topography, agro-chemicals supply and climate change. These issues significantly hinder agricultural productivity and the nations GDP (Yogi et al., 2025). The application of modern technologies in the agricultural sector presents the opportunity to transform the traditional agriculture system into agro-industrialization, which can effectively overcome trade deficits, food insecurity, income generation, poverty eradication and employment creation (Paudel, 2016). Technology and tools must be accessible to more localized, small-scale farmers and be more people-friendly to bring change in agricultural modernization paradigm (Sapkota, 2023).

Farmers in Nepal holding small and fragmented cultivable land practice manual traditional methods, where spraying of pesticide for prolonged time and large area require effort and possess significant health hazard. Direct exposure to pesticide and agro-chemicals can cause several health risks like, dermatological disorders, respiratory illness, neurological damage and in severe cases, even death (Karki & Dangol, 2023). Manual spraying is inefficient, time-consuming, uneven spray coverage and limits the area treated per day increasing the total cost while reducing overall crop protection effectiveness.

The development of UAVs in the field of agriculture in the recent years is regarded as a potential alternative to address the limitations of traditional methods of farming. With the application of drone technology, agriculture has become much safer and more productive. The technology possesses the potential to transform the economic model of farming and precision agriculture to make it accessible even for small-scale production (King, 2017.). Drones can be developed to perform automated tasks like crop health monitoring, weed management, evaporative transpiration estimation and pesticide spraying applications aiding to reduce human labor and increase the overall crop quality and productivity (Dutta & Goswami, 2020).

Nepali farmers depend primarily on food crop cultivation and small scale cash crops owning small cultivable plot of land (<0.6 ha) and fragmented farmlands. Accessibility of modern tools to such farmers and the use of UAVs in precision agriculture and pesticide spraying can significantly benefit to boost their income and reduce health risks associated with manual work. Application of drones for spraying pesticides reduce farmers' exposure to harmful chemicals, save time and labor and ensure uniform and effective pesticide application. The focus of the government to subsidize the development of agricultural technologies ensures a practical way to modernize agriculture, improve productivity and promote sustainable growth across the nation.

1.2 Problem Statement

Through the literature review and the study of feasibility for development of agricultural drones in Nepal, we found several problems and a few of them are mentioned as:

i. High cost of purchasing and the lack of a shared drone service model that makes spraying drones inaccessible to most Nepali farmers.
ii. Small (<0.6 ha) and fragmented landholdings prevalent among Nepali farmers reduce the operational efficiency and economic viability of agrochemical spraying.
iii. Pre-existing drone spraying systems are not terrain-adapted to the terraced and uneven field surface of Nepal, where spray drift and uneven coverage pose a significant challenge.

In addition to these primary issues, challenges like a lack of a clear regulatory framework for the use of drones in agriculture, as well as limited infrastructure and technical expertise for drone operations, maintenance and repair persist in Nepal. Most agricultural drones are operable for 15 - 20 minutes, which hinders the feasibility of use in rural and remote areas.

1.3 Scope of Work

The project titled *"Design and Fabrication of Pesticide Spraying Drone in Nepal "*involves the development of a functional prototype of a drone (0.5L capacity) specifically tailored for the small-scale farmers (<0.6 ha) in Nepal's hilly and terraced cultivating land. The scope of work includes:

i. Literature review of pesticide spraying drones, its challenges, design and development.
ii. Design a custom (0.5L capacity) drone frame, model using SOLIDWORKS and structural analysis using ANSYS to ensure strength and reliability.
iii. Identification and procurement of cost-effective essential electronic components.
iv. Develop a custom spraying mechanism to minimize drift loss and maximize coverage focused on uneven and terraced of Nepal.
v. Fabrication and assembly of a pesticide-spraying drone.

1.4 Objectives

The objectives of the project are divided into main objectives and specific objectives as mentioned below:

Main Objective:

i. To design and fabricate a functional drone capable of spraying pesticides, tailored to smallholder farmers in Nepal.

Specific Objective:

i. Study the endurance of a pesticide-spraying drone with a capacity of 0.5 liters for hilly and terraced fields.
ii. Study the spray performance and analyze the spray coverage using water-sensitive paper and drift loss evaluation.

1.5 Limitations

The limitations of our project are as follows:

i. Comparative testing with commercial agricultural application drones.
ii. Legal and regulatory compliance framework regarding pesticide spraying drone operation.
iii. Long-term performance testing under varying seasonal and weather conditions.

CHAPTER 2: LITERATURE REVIEW

This chapter explores the past literature and research efforts related to pesticide spraying using Unmanned Aerial Vehicles (UAVs). The chapter covers the key developments, technologies and findings in related fields, which provide solid foundations for understanding the progress made and identifying the gaps that this project aims to address.

(D., 2015) Drone-mounted sprayers are emerging as a crucial technology to address an increasing demand in food production by the efficient application of pesticides in agriculture. The developed drone was used to evaluate field capacity for groundnut and paddy crops, which showed an average field capacity of 1.15 ha/h and 1.08 ha/h, respectively, at a forward speed of 3.6 km/h and a spray height of 1m. The operational costs for groundnut and paddy crops were Rs 345/ha and Rs 367/ha, respectively. Laboratory tests reported a Volume Median Diameter (VMD) of 345 µm and a Number Median Diameter (NMD) of 270 µm for spray droplets. The drone is claimed to be essential for accessing crop fields that are inaccessible to humans, such as rice fields and orchards.

(Shaw & Vimalkumar, 2021) The World Health Organization (WHO) estimates that manual spraying causes one million pesticide-related diseases each year. An octocopter-shaped drone was created to solve this problem. It has a 12V pump, a 6L tank, four nozzles, eight BLDC motors (which can propel 38.2 kg) and a 22.2V, 22000mAh Li-Po battery. Carbon fiber (arms), polyethylene (tank) and carbon/Kevlar composite (base plate) were used for fabrication. They suggest that using drone-mounted spraying systems in agricultural fields can reduce the risk posed to personnel directly involved in spraying and also suggest using such systems for spraying disinfectant liquids over buildings, water bodies and highly populated areas. Future enhancements could be done to incorporate image processing for crop monitoring and GPS-based autonomy.

(Oktay et al., 2020) performed the CFD of a quadrotor to study the relationship between airspeed and propeller thrust coefficient utilizing a SST k-ω turbulence model. Incompressible and turbulent flow assumptions were made to solve the computational domain with the overset mesh technique. The results depicted that the thrust coefficients reduced at higher speeds and followed a similar trend to that of experimental results.

The generated mesh possessed a maximum skewness of 0.71 and a minimum orthogonal quality of 0.34. The tip speed of the propeller was calculated at 0.213 Mach number at 5000 rpm. The physics of the solver was based on sea-level conditions and solved for convergence of the order of 1e^-04. The discrepancy between simulated and experimental results ranged between 14-18%.

(S et al., 2021) focuses on designing a low-cost quadcopter to help small-scale farmers spray pesticides and fertilizers more safely and efficiently. Traditional spraying methods can be harmful to farmers and take a lot of time. The team collected feedback from farmers designed the drone using SolidWorks and tested its strength with ANSYS software. They built the drone using lightweight materials. The final drone can fly for about 7.4 minutes, carry up to 1200 grams and is easy to handle. It helps reduce health risks, saves time and can be used in hard-to-reach places like rooftop gardens and large trees. This work shows that drones can be a simple and affordable solution for modern farming.

(Saric et al., 2021) designed and analyzed the performance of a hexacopter using an analytical approach and validated the results through numerical analysis using the Finite Element Method (FEM). The study focused on evaluating the structural performance of the hexacopter during take-off and landing. The comparison between analytical calculations and FEM results showed a deviation ranging from 3% to 15%. The discrepancy was mainly due to the presence of singular points occurred due to insufficient refinement of finite element mesh. Another contributing factor was the simplification used in the analytical model where the take-off and landing mechanism was approximated as a cantilever tube clamped at one end with a load applied at the other end. Additionally, the deviation was also attributed to uncertainties in the material properties used in the FEM model due to limited available information.

(Butt et al., 2022) comprehensive review depicts that drones are widely used in the field of agriculture for crop monitoring, seeding, irrigation and more predominantly spraying pesticides. Along with the benefits like reduced human labour, precise and smooth operation, there are challenges such as less flight time, difficulty in balancing a drone with a pesticide tank and maintaining stability during harsh weather conditions. Also, for large-scale operations, drones are less efficient and costlier than other traditional aircraft or ground sprayers.

(Sambaiah et al., 2023) evaluated the performances of ANGRAU - PUSHPAK hexa-copter UAV in managing aphids, Myzuspersicae, on chilly with a 25 L / ha pesticide spraying rate. The hexacopter demonstrated efficacy in controlling aphids covering plants without missing areas or excessive drifts compared to traditional ground-based spraying methods. This study highlighted the application potential of UAVs in precision agriculture.

Different hover loads ranging from 0 to 5kg were numerically simulated to observe the downwash due to rotors. Increasing the load increased the airflow velocity of the downwash and the results appeared 11% error in z-axis velocity between measured and simulated velocities. The detailed analysis of the downward wind field led to a conclusion of a spray height of 2.5m or higher and the nozzle to be placed exactly under the rotors. The trumpet phenomenon appears in the downwash airflow area due to the rotation of the rotor and the extrusion of external atmospheric pressure. The y+ value of each rotor wall was maintained below 20 and rotor lifts seemed close to design values, ultimately increasing the accuracy of the numerical calculation of downwash. Turbulent flow of downwash due to inter-wing interference was caused by the counter-rotating motion and velocity of the adjacent rotors (Zhang et al., 2023).

Computation of Aerodynamics around the propeller region is crucial with the fast-growing industry of UAVs and drones. 3D compressible unsteady RANS of the flow was investigated around a 11- inch propeller using a CFD software. An open source software, QBlade was utilized to employ Blade Element Momentum Theory (BEMT) and calculate thrust forces and propeller torque at different revolutions, finally subjecting it to a wind tunnel test. The results depicted a 10% variation of the experimental results as compared to the CFD results. This suggested increasing rotating regions and refining mesh resolutions to address aeroacoustics as a future scope of work. Small-scale propellers ranging 6-22 inches in size function within a Reynolds number range of 30000-300000. The flow was computed for a rotation of 8000 rpm and maintained a y+ value of 3.5. Lower free stream velocities result in higher thrust coefficients for each rotational speed of the propeller (Fejes, 2024).

(Gurugubelli et al., 2023) presents the design and development of a multipurpose drone. The drone is lightweight, 3D-printed using PLA material, and designed for easy assembly and transport. It uses an Arduino and MPU6050 sensor for flight control and a GPS module was used to make it more stable and for positioning. Structural analysis was done using ANSYS to ensure the drone can handle real objects. Payload capacity of around 1 kg and flight time ranging from 2 to 9.6 minutes, the drone is suitable for various small-scale applications. The paper highlights the drone's low cost and suitability for multiple fields of application.

(Kavya & Shirwal, 2024) showed that droplet size is a critical factor for pesticide application using UAV. Impact of various spray parameters was conducted on droplet size during paddy spraying. Different nozzle types (flat fan nozzle, hollow cone nozzle and spinning disc nozzle), operating at varying forward speeds (2, 3, 4, 5 and 6 m s-l) and spray heights (l, 1.5, 2, 2.5 and 3 m above the crop canopy). This report suggests the significant effect on the droplet sizes depend on nozzle types, height and forward speed showed insignificant changes to droplet sizes. The study demonstrated that the nozzle type significantly changes the droplet sizes but forward speed didn’t change the average droplet sizes but downwash air flow of the drone-mounted sprayer breaks up the droplets into smaller sizes when the height increases but it does not significantly change the average droplet size. Based on the droplet sizes the flat-fan nozzle produced the largest droplets followed by the cone shaped nozzle, followed by the spinning disc nozzle. Flat-fan nozzle was selected which has a minimum drift due to its large sizes droplets.

(Gutierrez-rivera et al., 2024) article presents design, FEA and construction of a 30 kg hexacopter with a Nylamid motor bracket, aluminum sandwich-type skeleton and carbon fiber tube arm for precision agricultural applications, maintaining a thrust-to-weight ratio of 1.65. There are challenges regarding autonomy and the construction of agricultural drones, as it requires vigorous testing and proper flight dynamics. It was found that the use of materials like Nylamid can accelerate the manufacturing process of drone parts by up to 69% and reduce weight by 51% compared to aluminum, in light-duty CNC machines. Similarly, sandwich-type skeletons were found to be particularly effective in the early development stages due to their mechanical simplicity, fast implementation and testing. FEA was proven to be a powerful tool to correctly size the structures to comply with the design requirements of drone agriculture applications. Modal analysis of the drone parts was conducted to observe deformations due to natural frequencies and modes of vibration induced by rotating propellers. Vibration induced on the drone frame was measured by the accelerometer of the flight controller and it amounted to a value of 9.31 m/s2, which is below a 15m/s2 mark. The variance of 1% during simulations was considered for the grid independence and convergence of the solution. The flight data of the first flight for a hover time of 1-minute shows high stability of the drone with a total take-off weight of 37 kg. It highlighted the possible area of research regarding extensive mass optimization to compete with traditional light UAV skeletons.

(Öztürk et al., 2024) performed parametric optimization of structural frame design of a hexacopter for increased flight time and payload capacity. The hexacopter frame model was simplified and key geometric parameters like radii of slots and thickness of base plate were defined for the optimization. Finite element analysis was used to evaluate the stress and deformation of the frame under various design scenarios. The payload was 20 kgf, while each propeller had 3.5 kgf lifting capability and the material of the components was Al 6061 T6. The maximum Von Mises stress was found to be 64 MPa, which is about one-quarter of the yield strength. The maximum deformation was also below 0.3 mm and deformation under 1 mm is considered safe in the literature. The results showed that parametric optimization successfully reduced the weight of the hexacopter frame while maintaining structural integrity.

Advancements in additive manufacturing have led to the development and production of complex structures and products. The unconstrained structures, such as drones, satellites and airplanes, have complex designs and need advancement in optimization techniques where inertial relief can play a crucial role for optimal designs. The inertial properties of the structure are leveraged and concentrated non-structural masses are considered to find an optimum solution. The mathematical method of topology optimization helps to determine the optimal material distribution for a given design structure. The study depicts the comparison between boundary condition designs and inertial relief designs and also a combination of both. The inertial relief optimized designs have resulted in 12%-32% lower stress values as compared to those of boundary condition designs (Javier et al., 2025).

(Talaeizadeh et al., 2025) presents a comprehensive review on various types and structures of spraying drones, their dynamics modeling, control strategies, path planning, swarm control methodologies and droplet decomposition processes. This paper addresses the gap among various types and structures of drones available in the market. The paper provides criteria for selecting appropriate drones for specific agricultural applications. The review also traces human history from the Neolithic Revolution to the modern technological era and how UAVs ease various tasks in farming. The paper further introduces worldwide regulations, the challenges and future aspects of UAVs in the modern agricultural revolution.

(Akele & Akele, 2025) study presents the optimization of a hexacopter drone frame through generative design in Autodesk Fusion 360, intended for agricultural spraying applications. It enabled the identification of overstressed regions leading to iterative material removal and geometric refinement. The final drone frame had a mass of 2.784 kg achieved using ABS plastic via FDM 3D printing. The mass reduction transitioned from 7.2% to 38.1% compared to traditional 10-liter agricultural drone frames while maintaining a high safety factor range of 9.60 to 15 and a maximum displacement of just 1.288 mm. Additionally, flight performance analysis indicated a reduction in throttle requirement from 80% to 32.6% as tank weight decreased from 16.88 kg to 6.88 kg and hence extending flight duration from 6 to 14.6 minutes. These results demonstrated the effectiveness of generative design for developing structurally efficient and operationally robust UAV frames.

A steady-state MRF approach was employed to examine the velocity field and shear stress produced by the propeller jet. 10 inflation layers were imposed near wall to capture strongly changing gradient fields. SST k-ω and realizable k-ε turbulence models were compared on its sensitiveness to solve the models effectively. Differences in details of the shear stress values were uncovered which depicts the importance of appropriately selecting a mesh configuration and the turbulence model. The inflation layers were so added that the y+ was maintained below a value of 5 supporting a local refinement near wall zones. The persistent challenges of simulating bed shear stress and near bed velocity fields responsible to understand the initiation of scour is addressed by the author with comparison of the two turbulence models (Mahir & Ozan, 2026).

(Anken et al., 2024) showed that comparison of different nozzle (flat fan, hollow cone, air induction nozzles) produced almost similar distribution patterns in all the three measurement methods (Patternator, Filter Paper, Water Sensitive Paper). The injector nozzle with the largest droplets produced the best transverse distribution with coefficient of variation less than 10% by flat fan nozzle with a 120º spray angle that produced coarse droplets. It suggests that the consistent distribution attained only by overlapping working widths which is similar in size to the UASS (Unmanned Aerial Spray Systems).

CHAPTER 3: MATERIALS AND METHODOLOGY

The design and development of the Pesticide Spraying Drone followed a series of sequential process beginning with the identification of problem to a working design. This chapter outlines the details of material selection, design and testing of the fabricated drone each crucial for proper function and reliability during its course of use.

3.1 Materials

The project was focused on designing and developing the pesticide spraying drone utilizing locally available resources. Lightweight materials capable of enduring induced forces were considered during the design phase those meeting the design criteria. Engineering parameters like density, strength and reliability would directly affect the performance and stability of the drone. Proper selection of electronic components is equally significant as the drone solely relies on them for controls, maneuver and performance. The major components of the drone and selected materials are discussed below:

3.1.1 Mechanical Components

i. Frame:

The structure of the pesticide-spraying hexacopter was designed to be fabricated using Aluminium alloys. Plates of Aluminium alloy 6061, having thickness of 3mm was selected as the material of centre plates and square pipe of Aluminium alloy 6063 was selected as the material of arms. The aluminium alloys are easily available on the market and possess a reasonable strength-to-weight ratio. These alloys have tensile strength in the range of 0.1-0.3GPa, are highly durable and relatively easier to fabricate. The drone arms are fastened to the drone structure with nut bolts of 3mm diameter providing sufficient strength and rigidity to the drone frame.

ii. Propellers:

Propellers are the crucial components of avionics design affecting fundamental parameters of drone viz. lift forces, current consumption, rotational speed of the motors, drone speed and much more. The propellers account to the overall performance of drone affecting stability and maneuverability of the drone. Selection of a lightweight propeller operating on low vibrations is crucial to efficiently operate the drone. Thus, 15-inch Carbon Fiber propellers of 5.5-inch pitch were selected for the hexacopter drone delivering enough power and thrust requirements. Lightweight yet high strength property of the Carbon fiber propeller makes it able to withstand impacts and mechanical shocks. The specifications of the propellers are given in Table 1.

Material	Carbon fibre
Diameter	15
Pitch	5.5

Table 1: Specifications of Propellers

iii. Tank:

The pesticide-spraying drone is integrated with a 0.5L pesticide holding capacity tank built from lightweight polyethylene material. The tank weighs 103 grams and is mounted with a vent to circulate air, a passage to fill with pesticide and an outlet to feed the pump. The design of the tank contains baffles incorporated in its volume to minimize turbulence created by liquid waves.

iv. Spray nozzle:

Locally available adjustable cone-type nozzles of 1.5mm diameter were selected for the spraying system. A comparison of available nozzles in the market led us to the selection of this nozzle, fulfilling the spraying necessities of the pesticide spraying drone.

Figure 1: Aluminium Frame

Figure 2: Nozzle

Figure 3: Pesticide Tank

Figure 4: 15x5.5 Propellers

3.1.2 Electronics Components

The overall performance and functionality of the drone is dependent on the performance of electronic components marking it a significant aspect of drone design. The reliability of electronic components over a wide range of testing parameters is important during the testing and development phase. Thus, proper study of electronic components was conducted which led us to the selection of following components.

Figure 5: Electronic Speed Controller

Figure 6: BLDC Motors

Figure 7: GPS Module

Figure 8: Power Module

i. ESC-40A:

. The specifications of ESCs are presented in Table 2.

Item Type	Brushless ESC
Burst Current (A)	60
Constant Current (A)	40
BEC (Y/N)	(5V/3A), Yes
Compatible Li-Po Batteries	2S to 4S
Color	Black
Dimensions (L x W x H) mm	7 x 3
Weight (g)	34

Table 2: Specifications of ESC

The Electronic Speed Controller(ESC) controls the power delivery and regulates the speed of the motors, tweaking current and voltage parameters. Considering a safety factor of 1.6, 40A-rated ESCs were selected to control motors rated at 25A

ii. 5010 BLDC Motor (750 kV):

The pesticide spraying drone demands a high thrust to weight ratio sufficient to handle payload capacity and liquid turbulence. BLDC 750kv high-torque motors are capable of delivering about 1400 grams of thrust at full load sufficiently large enough to maintain the thrust to weight ratio. These motors can efficiently generate torque and transmit motion to the hexacopter drone capable of about 11000 revolutions at no load. The specifications of the 5010 750kv brushless DC motors are presented on table 3.

Motor KV (RPM/V)	750
Motor Type	Brushless Motor
Compatible Li-Po Batteries:	2S to 6S
Required ESC (A)	20 ~ 40
Maximum Thrust (gm)	1500@4S
Shaft Diameter (mm)	4
Compatible Prop (inch)	14 ~ 16
Length (mm)	50
Width (mm)	50
Height (mm)	10
Weight (g)	112

Table 3: Specifications of 750kv BLDC Motor

iii. Battery 4S - 25C LiPo 13000mAh:

The specifications of the battery are presented on table 4.

Nominal Voltage (V)	14.8
Nominal Capacity (mAh)	13000
Discharge Current	25C
Battery Cell Configuration	4S
Balance Plug	JST-XH
Discharge Plug	XT60
Length (mm)	170
Width (mm)	70
Height (mm)	40
Weight (g)	1020

Table 4: Specifications of LiPo Battery

The drone comprises of high torque motors that operate at high current and consume more power. This intensifies the need of a suitable power supply capable of delivering a continuous high amount of current throughout the flight. A 4S LiPo battery rated at 14.8V 13000mAh was selected to power the system and to achieve a total flight time of five minutes at full load.

iv. Pixhawk 2.4.8:

The open-source flight controller Pixhawk 2.4.8 was selected to control and operate the drone. The flight controller can be easily updated with required firmware of the drone and calibrated for stable flights. The flight controller provides ease of use and the interface of mission planner is easy to comprehend making it easier to configure changes in the system. This flight controller is based on Nux processor and RTOS as an operating system.

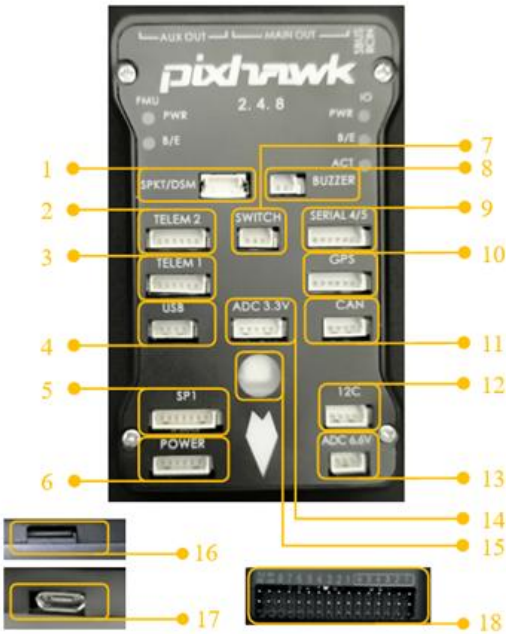

Figure 9: Pixhawk 2.4.8

1. Spektrum DMS receiver
2. Telemetry (on-screen display)
3. Telemetry (radio telemetry)
4. USB
5. SPI (Serial Peripheral Interface) bus
6. Power module
7. Safety switch button
8. Burger
9. Serial
10. GPS module
11. CAN (Controller Area Network)
12. I2C splitter or compass module
13. Analog to digital converter 6.6V
14. Analog to digital converter 3.3V
15. LED indicator
16. SD card slot
17. Micro USB port

vi. Relay Switch:

The drone is equipped with a centrifugal pump to deliver pesticides to the spraying nozzles. A customized relay switch was adopted to control and operate the pump manually through the transmitter.

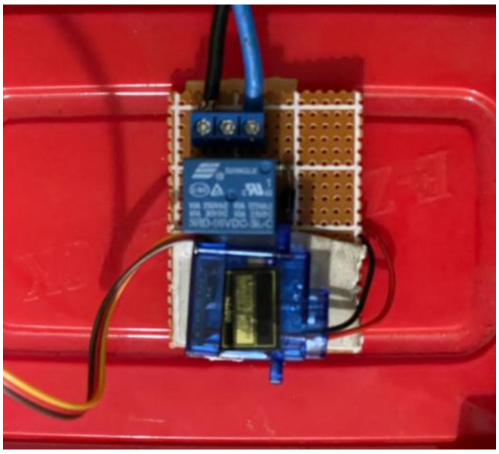

Figure 10: Relay Switch

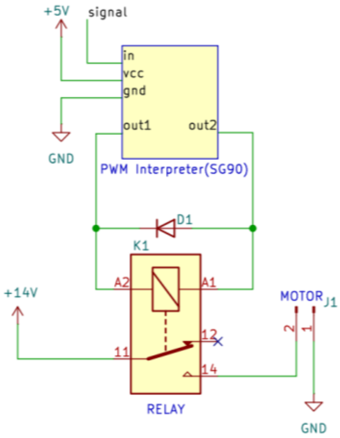

Figure 11: Schematic of the Relay switch

vii. GPS

The specifications of the selected GPS are presented on table 5.

Model Name:	Ublox NEO-M8N
Receiver Type	72-channel Ublox M8 engine.
Main Chip	Ublox NEO-M8N
Position Accuracy (Meter)	2, 2.5
Acceleration (g)	<4
Navigation Update Rate	up to 18 HZ.
Operating Temperature (°C)	-45 to 105
Tracking Sensitivity (dBm)	-161 dBm
Avg Cold Start Time (s)	30
Warm Start Time (s)	1
Additional Specs.	Boot Time: 1S, Capture Time: 0.1s Average, Co-Ordinate System: WGS-84
Maximum Altitude (m)	18000
Weight (g)	33
Cable Length (cm)	20
Input Voltage (V)	0.5 to 3.6
Dimensions (L x W x H) mm	54 x 22 (Dia x W)

Table 5: Specifications of GPS

The GPS module is a crucial part of the drone, contributing to the stability and locating the position of the drone. The orientation of the drone can be manipulated using data from its compass and accelerometer and is highly efficient in utilizing PID.

viii. Power Module:

A power module of 90A current-sensing capacity applicable for the flight controller was selected. The power module is utilized to power the flight controller with 5V and supply the PDB with 14.8V.

Operating Voltage (VDC)	6 to 28
Voltage Rating (V)	5
Input Voltage (VDC)	28
Current-Sensing(A)	90
Connector Type	XT60
Length (cm)	160
Weight (g)	24

Table 6: Specifications of Power Module

ix. Radio transmitter

A 10-channel Flysky Fs-i6 transmitter having a range of 1km was selected to maneuver the drone transmitting PWM signals to the receiver. The specifications of the transmitter are presented in table 8.

Channels	10
RF range	2.408 - 2.475GHz
Bandwidth	500 KHz
Bands	135
RF power	Less than 20 dBm
Protocol	AFHDS 2A
Modulation type	GFSK
Stick resolution	4096
Low voltage alarm	Yes (lower than 4.2V)
PS2/USB Port	Yes (Micro-USB)
Power input	6V DC 1.4AA*4
Weight	392g
Size	174*89*190 mm

Table 7:Specifications of Radio Transmitter

x. Power Distribution Board:

The power distribution board (PDB) supplies power to the ESCs and the sprayer pump. An eight-channel PDB capable of handling up to 20A at each outlet was selected, whose specifications are presented in Table 7.

Material	Glass Fibre
Channels	8
Plug	XT60
Dimensions	50x50x2 mm

Table 8: Specifications of PDB

xi. Radio receiver

The default 10-channel receiver of the Flysky Fs-i6 was selected as the radio receiver of the drone to transfer PPM signals to the Pixhawk flight controller. The specifications of the radio receiver are presented in Table 9.

No. of Channels:	10
No. of Bands	140
Modulation Type:	GFSK
RF Range	2.4055–2.475 GHz.
Sensitivity (dBm):	-105
Signal Output	IBUS, PPM
Operating Voltage (VDC):	4.0 ~ 6.5
Current Consumption (mA):	≤40
Control Distance	400m+
i-Bus Interface	Yes
Antenna Gain	2dB
Antenna Length (mm)	110
Weight (g):	15

Table 9: Specifications of Radio Receiver

3.2 Methodology

The design and development of the pesticide spraying drone followed a series of steps as shown in the Methodological chart of figure 12. The design methodology began with the identification of the problem followed by its literature review enabling the development of preliminary designs.

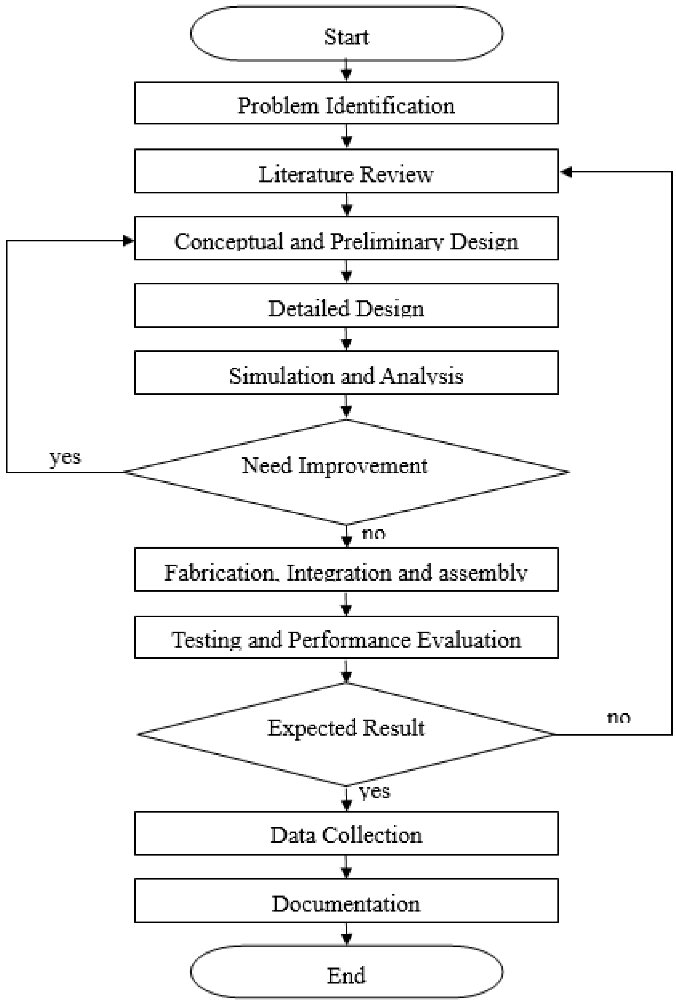

Figure 12: Methodological Chart

The forces and weights of components acting on the drone structure were calculated during the preliminary design phase. The total take-off weight with a payload capacity of 0.5N was calculated to be around 48N. This led to the selection of a hexagonal configuration designed to have a thrust-to-weight ratio of 1.6 ensuring smooth maneuverability of the drone. Aluminium alloys 6061 and 6063 having a density of 2700kg/m3 were selected as materials for base plates and arms respectively based on their availability and strength. A conceptual model of the desired hexa-copter was modeled on SolidWorks paving a path to drone development. The mechanical and electronic components were selected based on design requirements to be integrated on the drone frame. The final design and calculations of the drone was formulated and remodeled on SolidWorks. The model was analyzed on ANSYS, a FEA solver for structural integrity. This followed the removal of unwanted weight of least stressed areas from the drone structure to reduce the weight as a part of topology optimization.

The selected components were procured and mechanical components were machined to facilitate the fabrication of the hexacopter. The machined Aluminium plates and arms were assembled to provide the structure of the drone with electronic components mounted on it. The designed tank was connected to a two nozzle sprayer system deployed for spraying purpose fed by a centrifugal pump. A connection is established between the electronic components to complete the circuit and develop communication. The hexacopter spraying drone underwent vigorous testing for performance and stability finally contributing to the documentation of the project.

3.3 Design and Calculations

The design of the X-configuration hexacopter drone is based on the theories of multi-rotor UAV design. Each adjacent rotor has opposite rotation to balance the aerodynamic torque and cancel the gyroscopic effect in a trimmed flight (Rizon et al., 2020).

3.3.1 Hexacopter Kinematics

The rigid body kinematics of the hexacopter drone can be parametrized using Newton-Euler method. The free body diagram of the hexacopter drone with its coordinate system is depicted in figure 13.

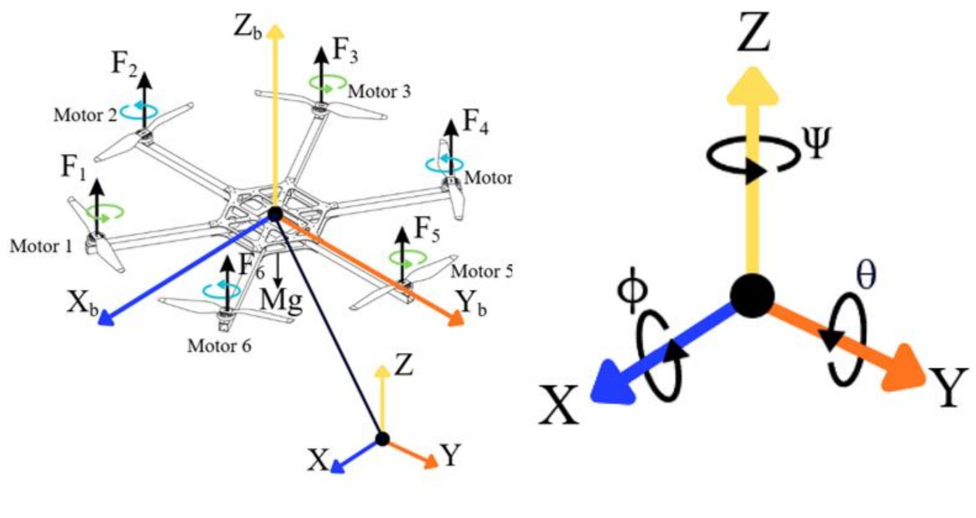

Figure 13: Drone Coordinate System

The fixed frame of reference is considered as an inertial frame defining the absolute linear position of a hexacopter as (X, Y, Z). The mobile body frame of reference (X_b,

Y_b, Z_b) is defined at the center of gravity of the hexacopter. The orientation of the hexacopter with respect to the inertial frame is defined by Euler angles roll Φ, pitch θ and yaw Ψ. The inertial position vector and Euler angle vector are denoted as $\xi = [x\ y\ z]^T$ and $\eta = [\Phi\ \theta\ \Psi]^T$ respectively (Moussid, 2015). Where $\Phi, \theta\ \in \left(-\frac{\pi}{2}, \frac{\pi}{2}\right)$ and $\Psi \in (-\pi, \pi)$ to prevent ambiguity and gimbal lock (Sanca et al., 2010). Based on Euler angles representation and right-hand coordinate conventions, the roll angle rotation matrix about the x-axis:

$$R(x, \Phi) = \begin{bmatrix} 1 & 0 & 0 \\ 0 & c(\Phi) & -s(\Phi) \\ 0 & s(\Phi) & c(\Phi) \end{bmatrix}$$

the pitch angle rotation matrix about the y-axis:

$$R(y, \theta) = \begin{bmatrix} c(\theta) & 0 & s(\theta) \\ 0 & 1 & 0 \\ -s(\theta) & 0 & c(\theta) \end{bmatrix}$$

and, the yaw angle rotation matrix about the z-axis:

$$R(z, \Psi) = \begin{bmatrix} c(\Psi) & -s(\Psi) & 0 \\ s(\Psi) & c(\Psi) & 0 \\ 0 & 0 & 1 \end{bmatrix}$$

The transformation from the body frame to the inertial frame of reference can be realized using a complete rotation matrix, called the direction cosine matrix R (Ibrahim et al., 2017).

$$R_B^E(\Phi\ \theta\ \Psi) = \begin{bmatrix} c(\Psi)c(\theta) & c(\Psi)s(\theta)s(\Phi) - s(\Psi)c(\Phi) & c(\Psi)s(\theta)c(\Phi) + s(\Psi)s(\Phi) \\ s(\Psi)c(\theta) & s(\Psi)s(\theta)s(\Phi) + c(\Psi)c(\Phi) & s(\Psi)s(\theta)c(\Phi) - c(\Psi)s(\Phi) \\ -s(\theta) & c(\theta)s(\Phi) & c(\theta)c(\Phi) \end{bmatrix}$$

Where c indicates cos(), s indicates sin() and t indicates tan() in the equations.

The linear velocity acting on the hexacopter body $v = [v_x, v_y, v_z]^T$ is related with respect ot inertial frame velocity $V = \begin{bmatrix} \dot{P}_x & \dot{P}_y & \dot{P}_z \end{bmatrix}^T$ as:

$$\begin{bmatrix} \dot{P}_x \\ \dot{P}_y \\ \dot{P}_z \end{bmatrix} = R(\Phi\ \theta\ \Psi) \begin{bmatrix} v_x \\ v_y \\ v_z \end{bmatrix}$$

The angular velocity of a hexacopter body with respect to the body frame $\omega = [\, p\; q\; r]$, called gyroscopic rate, is related to the time derivative of the Euler angle $[\dot{\Phi} \quad \dot{\theta} \quad \dot{\Psi}]$ as:

$$\begin{bmatrix} \dot{\Phi} \\ \dot{\theta} \\ \dot{\Psi} \end{bmatrix} = \begin{bmatrix} 1 & s(\Phi)t(\theta) & c(\Phi)t(\theta) \\ 0 & c(\Phi) & -s(\Phi) \\ 0 & s(\Phi)\sec(\theta) & c(\Phi)\sec(\theta) \end{bmatrix} \begin{bmatrix} p \\ q \\ r \end{bmatrix}$$

3.3.2 Hexacopter Dynamics

The thrust generated by rotating rotors is responsible to maneuver drone in a 3D space. The thrust must balance the payload takeoff weight(PTW) of the drone for a trimmed flight and compensate for active forces and moments incurred on the body. The movement of the hexacopter is governed by different physical, aerodynamic and mechanical processes, which are presented on Table 10.

Effects	Cause
Aerodynamics effect	Propellers rotations
Inertial counter torque	Speed change of propellers
Gravity effect	Center of mass position
Gyroscopic effect	Change in hexacopter orientation
Frictional effect	Movement of the hexacopter
Ground effect	Proximity to surface
Propeller-propeller interaction	Overlapping rotors vortex
Vibration effects	Structural oscillation
Control system effect	Latency and tuning of controller
Environmental disturbance	Wind, turbulence and temperature
Battery/power effect	Voltage sag and depletion

Table 10:Aerodynamic and Mechanical Effects on Hexacopter Dynamics

The hexacopter is assumed to be a rigid body to derive the equations of the motion. The thrust generated is considered to be proportional to the square of the propeller angular velocity (Moussid et al., 2015). The position equation for hexacopter is obtained by Newton-Euler formulation (Saleh & Aboukassem, 2018)(Fogelberg, 2013)for a rigid body as:

$$\begin{bmatrix} mI_{3\times3} & 0_{3\times3} \\ 0_{3\times3} & J \end{bmatrix}\begin{bmatrix} \dot{v} \\ \dot{\omega} \end{bmatrix} + \begin{bmatrix} \omega \times mv \\ \omega \times J\omega \end{bmatrix} = \begin{bmatrix} \sum F \\ \sum M \end{bmatrix}$$

Where m is the gross mass of the hexacopter body, I_{3x3} is an identity matrix, $0_{3\times3}$ is a zero matrix, $J_{3\times3}$is the inertia tensor which depicts how masses are distributed relative to the body coordinate axes.

The above equation provides translational and rotational dynamics for a hexacopter and upon expanding the equation provides linear and rotational acceleration of the body as:

$$\begin{bmatrix} \dot{v}_x \\ \dot{v}_y \\ \dot{v}_z \end{bmatrix} = \begin{bmatrix} rv_x - qv_z \\ pv_z - rv_x \\ qv_x - pv_y \end{bmatrix} + \frac{1}{m}\begin{bmatrix} F_x \\ F_y \\ F_z \end{bmatrix}$$

$$\begin{bmatrix} \dot{p} \\ \dot{q} \\ \dot{r} \end{bmatrix} = \begin{bmatrix} \frac{I_{yy} - I_{zz}}{I_{xx}} qr \\ \frac{I_{zz} - I_{xx}}{I_{yy}} pr \\ \frac{I_{xx} - I_{yy}}{I_{zz}} pq \end{bmatrix} + \begin{bmatrix} \frac{1}{I_{xx}} M_x \\ \frac{1}{I_{yy}} M_y \\ \frac{1}{I_{zz}} M_z \end{bmatrix}$$

A rotating propeller generates thrust force and the resisting torque generated is drag. The total thrust generated by the propeller $T = [0 \quad 0 \quad \sum_{i=1}^{6} F_i]^T$ and torque by momentum conservation (Sanca et al., 2010) is given by:

$$T = \sum_{i=1}^{6} F_i = \rho C_t A R^2 \sum_{i=1}^{6} {\Omega_i}^2$$

$$Q = \sum_{i=1}^{6} \tau_i = \rho C_Q A R^3 \sum_{i=1}^{6} {\Omega_i}^2$$

where Ω_i is the angular velocity of each propeller, A is the disk area, R is the propeller radius, T is the thrust generated by propellers, Q denotes the resisting torque on the rotor.

The thrust constant C_t and torque constant C_Q from the blade element theory(BET) is given by:

$$C_t = \frac{1}{4}\sigma C_{l\alpha}\left[\frac{2\beta_b}{3} - (\lambda_c - \lambda_i)\right]$$

$$C_Q = \frac{1}{2}\sigma\left[C_{L\alpha}(\lambda_c - \lambda_i)\left\{\frac{\beta_b}{3} - \frac{\lambda_c - \lambda_i}{2}\right\} + \frac{C_D}{4}\right]$$

Where,

$\sigma = rotor\ solidity$

$C_{L\alpha} = Lift\ slope\ coefficent$

$\beta_b = Propeller\ pitch\ angle$

$C_D = Chord\ length\ at\ r$

$\lambda_c, \lambda_i = Climb\ inflow, Induced\ inflow$

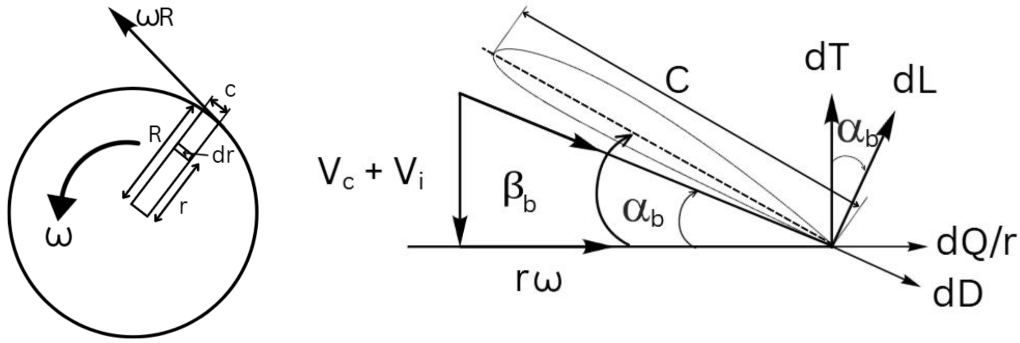

Figure 14: Blade Element Theory of a Propeller Blade

The gravity force acting on the body along the Earth's z-axis is given by:

$$F_g = R_E^B[0 \quad 0 \quad -mg]^T = -mg\begin{bmatrix} -s\ (\theta) \\ c(\theta)s(\Phi) \\ c(\theta)c(\Phi) \end{bmatrix}$$

Thrust and torque generation for hexacopter depend on the rotation of the relatively counter-rotating propellers. The independent motion of a hexacopter on 3D space depends on the dynamic action of a propeller generating thrust and torque about the body axis. Roll, pitch and yaw motion is obtained by the moment generated by the rotors placed away from the center of gravity and a particular axis of the hexacopter body as shown in Figure 15.

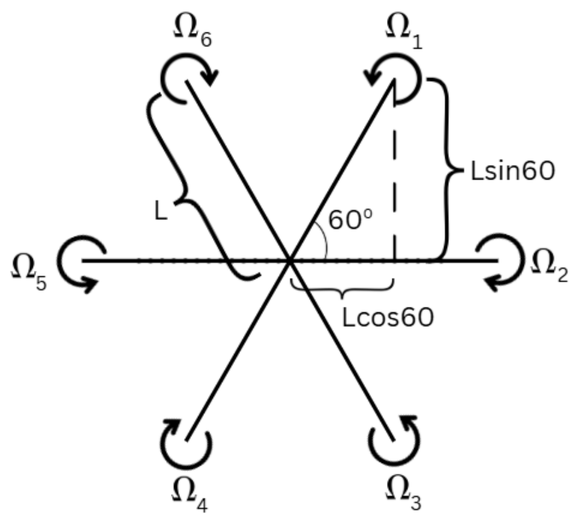

Figure 15: Hexacopter Dynamics

The torque produced on the body frame of reference is based on the right-hand convention. Positive roll torque is obtained by increasing the angular speed $\Omega_4, \quad \Omega_5, \quad \Omega_6$ and decreasing $\Omega_1, \quad \Omega_2, \quad \Omega_3$, which can be realized with the equation as:

$$\tau_{roll} = \rho C_t A R^2 L \left\{ -{\Omega_2}^2 + {\Omega_5}^2 + \frac{1}{2}\left(-{\Omega_1}^2 - {\Omega_3}^2 + {\Omega_4}^2 + {\Omega_6}^2\right) \right\}$$

Positive pitch torque is obtained by increasing the angular velocity $\Omega_3, \quad \Omega_4$ and decreasing $\Omega_1, \quad \Omega_6$ as provided by following equation:

$$\tau_{pitch} = \rho C_t A R^2 L \frac{\sqrt{3}}{2}\left(-{\Omega_1}^2 + {\Omega_3}^2 + {\Omega_4}^2 - {\Omega_6}^2\right)$$

Positive yaw torque is obtained by increasing the angular velocity of $\Omega_2, \quad \Omega_4, \quad \Omega_6$ and decreasing of $\Omega_1, \quad \Omega_3, \quad \Omega_5$, causing a resisting torque imbalance that creates a yaw movement and the equation can be realized as:

$$\tau_{yaw} = \rho C_Q A R^3 \left(-{\Omega_1}^2 + {\Omega_2}^2 - {\Omega_3}^2 + {\Omega_4}^2 - {\Omega_5}^2 + {\Omega_6}^2\right)$$

3.3.3 Material Selection

The available materials were compared based on their cost, availability, strength and weight to fabricate the structure of the drone. Aluminium was selected as a suitable material for the drone structure considering the aspects of comparison depicted in Table 11.

S.N.	Materials	Density (g/cm^3)	Tensile Strength (MPa)	Youngs Modulus (GPa)	Cost
1.	Al 6061 T6	2.70	240 - 310	68 - 71	Moderate Rs.2562 (3*200*200)
2.	ACP (Aluminum Composite Panel)	1.5 - 2	50 - 200	5 - 15	Low Rs. 850-1500 (3-6mm) (1260*1500)
3.	Carbon fiber	1.5 - 1.8	500 - 1500	70 - 150	Very High Rs.7279 (3*200*300)
4.	PVC Foam	0.03-0.20	1 -10	0.01 – 0.2	Low Rs.1710 (3*300*200)
5.	PLA (3D Printed)	1.34	40 - 70	2.5 – 3.5	Moderate Rs.2750 (1.75mm, 1kg)

Table 11: Comparison of Available Materials

3.3.4 Liftoff Weight Composition

S. N	Mechanical Components	Mass(in grams)
1.	Base Plate	263
2.	Top Plate	236
3.	Branch	513
4.	Battery Case Mount (3D Print)	41
5.	Nut Bolts	50
6.	Pesticide Box (1 Liter)	103
7.	Landing Gear	283
8.	Pump Mount	21
9.	PDB Mount	11
10.	Pesticide and landing mount	62
11.	Radio, Pixhawk, GPS mount	63
12.	Payload	500
13.	Spraying System	280
14.	Miscellaneous	84
Total		2510

Table 12: Mass Distribution of Mechanical Components

S. N	Electronics Component	Mass in grams
1.	GPS and GPS Stand	52
2.	Receiver	19
3.	Battery	1110
4.	Relay Switch	23
5.	Pixhawk	39
6.	Buzzer	4
7.	PDB and Power Module	20
8.	Motor (6 pcs)	564
9.	ESC (6 pcs)	252
10.	Propeller (6 pcs)	168
11.	Pump	109
Total		2360

Table 13: Mass Distribution of Electronic Components

A digital weighing machine was used to measure the masses of mechanical and electronic components presented on Tables 12 and 13 respectively. The total mass of the drone was calculated to be 4870 grams comprising 2510 grams of mechanical components and 2360 grams of electronic components.

3.3.5 Thrust to Weight Consideration

The thrust required for the drone to hover can be calculated as;

$$T_{hover} = gross\ mass\ of\ drone\ \times g = 4.87\ Kg\ \times 9.81\ m/s^2 = 47.7747\ N$$

Most of the agricultural drones have a thrust-to-weight ratio in the range of 1.6 to 2 for takeoff and flight maneuvers. To maintain the thrust to weight ratio of 2, the total thrust to be generated by the propeller is calculated as;

$$T_{total} = T_{hover} \times 2 = 95.5494\ N$$

So, the total thrust requirement is 95.5494 N

3.3.6 Drone Configuration Consideration

Quad, hexagonal and octagonal configurations are most commonly preferred configurations of the drone structure. The hex configuration is capable enough to provide enough thrust while maintaining stability of the drone during spraying activities. A hexacopter helps to enhance the thrust and provides fault tolerance due to its six rotor redundancy proving to be ideal for agricultural applications. The hexacopter structure aids stability with superior payload capacity providing structural integrity and redundancy. Thus, a hex-configuration was selected for the structure of the drone.

Figure 16: Comparison of Multirotor UAVs

3.3.7 Thrust Requirement of each Arm

The selection of a hex-configuration led us to six arms and six rotors. The thrust required for each propeller to maintain the thrust-to-weight ratio of 2 is calculated as,

$$T_i = \frac{Total\ Thrust}{Number\ of\ propellers} = 15.9249\ N$$

Hence, to maintain the ratio, each propeller needs to generate a 15.9249N force.

3.3.8 Motor Selection

The thrust of the propeller is derived from the rotation of the motors. The theoretical maximum rotational speed of the motors at no load can be calculated using the kv rating of the motors.

$$RPM_{no\ load} = K_v \times V$$

where,

K_v =Speed rating

V = Operating voltage

RPM with a loaded propeller is the actual rpm of the motor which creates aerodynamic drag and load torque, reducing the motor's speed.

$$RPM_{loaded} = \eta_{rpm} \cdot RPM_{no\ load}$$

Where, η_{rpm} = Motor efficiency factor

Thrust generated by a rotating propeller depends on the density of the air, rotational speed and the design and geometry of the propeller itself (Magnussen et al., 2015).

$$T_i = C_t \cdot \rho \cdot \mathrm{n}^2 \cdot D^4$$

Where,

C_t = thrust coefficient of propeller

ρ = density of air

n = rotor speed (rev/sec)

D = propeller diameter

The power supply required by a motor to spin the rotors is given by the propeller power equation (Magnussen et al., 2015). The rotation of propellers induces a certain torque as well.

$$W_{motor} = C_p \cdot \rho \cdot \mathrm{n}^3 \cdot D^5$$

$$\tau_i = \frac{W_{motor}}{\omega}$$

Where,

C_p = power coefficient of propeller (from datasheet)

ω = 2πn is the rotor speed (rad/sec)

High torque BLDC motors of 750kv rating each, capable of generating high thrust was selected based on its availability and affordable price.

3.3.9 Propeller Selection

The selection of the propeller was based on the theoretical calculation of the thrust it can generate with the pre-selected motor and power consumption considerations.

Speed rating (kV) = 750kV

Operating Voltage (V) = 14.8 V

Motor efficiency factor (η_{rpm}) = 0.75 (range 0.75 - 0.85)

Thrust coefficient of propeller (C_t)= 0.11 (in range 0.11 - 0.13)

Power coefficient of propeller (C_p) = 0.05 (in range 0.04 - 0.05)

Density of air (ρ) = 1.11 kg/m^3

At first, no load and loaded rpm were calculated for the BLDC motor as;

No load rpm = kV · V = 750 × 14.8 = 11100 rpm

Loaded rpm = η_{rpm} · kV · V = 0.75 × 750 × 14.8 = 8325 rpm

Motor speed (n)= rpm/60 = 8325/60 = 138.75rps.

Now, the propeller thrust for 15-inch propeller was calculated as;

$$T_{15"} = C_t \cdot \rho \cdot \mathrm{n}^2 \cdot D^4 = 0.11 \times 1.11 \times 138.7^2 \times 0.381^4 = 49.49\ N$$

Hence, thrust for a 14" propeller is 49.49 N (5.044 Kg.f)

$$W_{15"} = C_p \cdot \rho \cdot \mathrm{n}^3 \cdot D^5 = 0.05 \times 1.11 \times 138.75^3 \times 0.381^5 = 1190.91\ watt$$

and,

$$\tau_{15"} = \frac{W_{14"}}{\omega} = \frac{1190.91}{2 \times \pi \times 138.75} = 1.365\ Nm$$

Considering 75% efficiency of the motor (in the range 75- 85%)

$$Battery\ Power\ Supply(P_{15"}) = \frac{W_{15"}}{\eta} = \frac{1190.91}{0.75} = 1586.92\ watts$$

The above thrust can be generated by the propeller at the current drain of;

$$Consumed\ ampere\ (A) = \frac{1586.92\ watts}{14.8\ V} = 107.224\ amp$$

which exceeds the maximum current for the motor (25 Amp). Thrust generated by the propeller needs to be re-calculated with in the limit of motor requirements. Considering the factor of safety, take 22 amps of maximum current supply.

$$Battery\ power\ supply(P_{in}) = I \times V = 22\ amp \times 14.8\ V = 325.6\ watts$$

$$Mechanical\ power\ output(P_{out}) = \eta \cdot P_{in} = 0.75 \times 325.6 = 244.2\ watts$$

(η is assumed to be 0.75 which typically ranges in 0.75-0.85)

Since Rotor Power is the same as the mechanical power output, solving equation 5 with the new rotor power (P_{out}), we get;

$$n_{15"} = 81.84\, rps$$

hence, thrust at this rotation solving equation 6, we get;

$$\left(T_{15"}\right)_{new} = 17.23\, N$$

3.3.10 Thrust-to-Weight Ratio Validation

Total number of propellers = 6

Net thrust = 17.23 × 6 = 103.38 N

∴ Thrust to weight ratio = $\frac{10.54}{4.87} = 2.164$

15-inch propellers generated a thrust-to-weight ratio of 2.16 theoretically, thus making it a suitable choice for the hexacopter.

3.3.11 Length of Frame:

The counter-rotating adjacent propellers eliminate the moment that could create the Yaw movement of the drone. The length of the frame (L) depends on the propeller diameter (D) and the number of rotors used (N). The minimum interference gap between two propellers is given by the sine law. Considering the safety of the drone and to prevent aerodynamic interference greater value than the minimum length is considered.

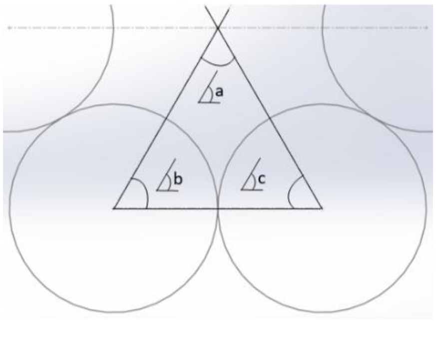

$$\frac{\sin(a)}{A} = \frac{\sin(b)}{B} = \frac{\sin(c)}{C}$$

$$L = \frac{D}{\sin(\pi/N)}$$

Figure 17: Sine Law

The Hex-X configuration as in figure 18, is preferred for the drone structure as it ensures a clear forward motion without interference of propellers. This setup allows for better payload mounting ensuring smoother and stable controls.

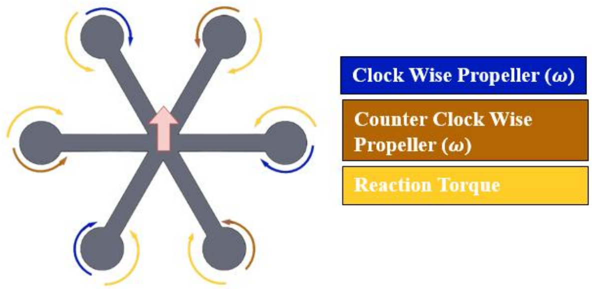

Figure 18: Hex-X Configuration

Drone frame length calculation was based on considering a safe spacing between 15-inch propellers. Initially the interference length between propellers in the worst case scenario was calculated and a proper gap was allocated between two propeller tips of adjacent rotors. The minimum length of the with propeller interference was calculated as:

$$L = \frac{D}{\sin(\pi/N)} = \frac{15}{\sin\,(\pi/6)} = 30\;inch = 762\;mm$$

For a 15-inch propeller, the adjacent Motor to Motor distance (MTM) is 381mm. Conventionally a gap of 3-5 inches is allowed between two adjacent propeller tips to avoid propeller interference. To avoid aerodynamic interference between propellers, the spacing ratio of 0.762 was considered, which lies within the range recommended by (Lei et al.,2020) and consequently, the adjacent rotor spacing was calculated as.

$$Adjacent\;rotor\;spacing(S) = \frac{381}{0.762} = 500\;mm$$

$$Wheelbase = 2 \times S = 1000mm$$

So, the final length of the wheelbase with this the spacing criterion was calculated to be 1000mm.

3.3.12 Stress Calculation:

Stresses are calculated at the junction of the base plate and the arm considering maximum thrust generated by the rotor at maximum power supply.

$$Thrust(T) = m \times g = 17.23\;N$$

Distance between the junction and point of action of thrust (r) = 0.321 m

$$Moment\;at\;frame\;and\;arm\;junction(M) = T \times r = 4.45Nm$$

For hexacopter arm cross-section;

a = 24 mm

b = 22 mm

y = 0.0127 m

$$Moment\ of\ Inertia\ (I) = \frac{1}{12}(a^4 - b^4) = 8.13 \times 10^{-9} m^4$$

$$Stress\ at\ A(\sigma) = \frac{My}{I} = 6.57\ \ N/mm^2$$

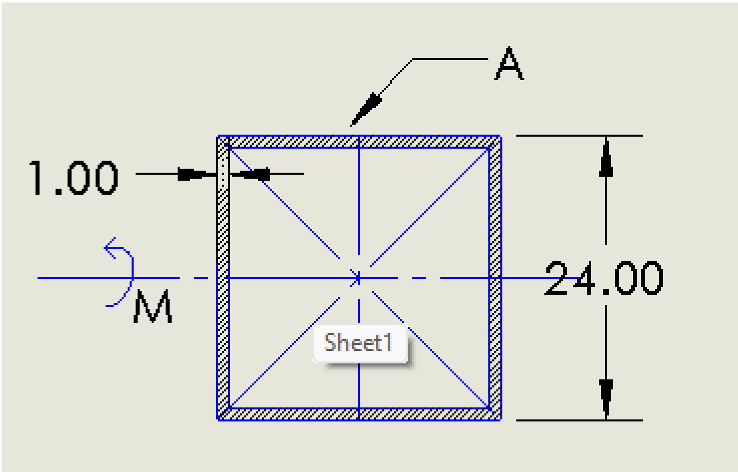

Figure 19: Cross Section of the Square Arm Tube

First moment of area of hollow square cross-section about its neutral axis;

$$Q = \sum A\bar{y} = 397\ mm^3$$

and shear force;

$$V = P = 17.23\ N$$

The transverse shear stress that develops in the beam due to a shear force acting perpendicular to the beam axis is calculated as:

$$Transverse\ shear\ stress\ (\tau) = \frac{V \times Q}{I \times t} = 420683.27\ \text{Pa} = 0.42\ \text{MPa}$$

This value is significantly lower than the typical shear strength of Aluminum 6061 (207 MPa), so it confirms that the design is safe from shear failure.

The drone experiences certain level of vibrations due to rotating components during flight. These frequencies need to be accounted and ensured that the natural frequency of the drone exceeds the excitation frequencies produced by the rotors. The excitation frequency due to the rotation of the motors is calculated as:

$$f_m = \frac{rpm}{60} = 177.6\ Hz$$

Considering the arm as a cantilever beam, the natural frequency of the arm is calculated as:

$$f_n = \frac{\beta^2}{2\pi}\sqrt{\frac{EI}{\rho A L^2}} = 281\ Hz$$

The landing gear of the drone must be analyzed to calculate its resistance to impacts and shocks to ensure safe landings. This can be evaluated considering the conversion of potential energy to kinetic energy at impact.

$$E_{impact} = mgh$$

Where, m = mass of the drone and h = landing height

For a drone of mass 4.87 Kg and 8 m fall, the energy at impact is 382.1976 J. This energy is to be resisted by the landing gears, whose geometry and material properties play a vital role in the structural integrity during landing. The stiffness of the leg having a length of 0.2m is calculated using the stiffness equation.

$$K_{leg} = \frac{3EI}{L^3} = 310.36\ KN/m$$

The total stiffness of the system comprising of four legs is K_{total} = 841.44 KN/m.

Assuming no energy loss and pure elastic deformation during landing, the maximum deflection of the landing gear is calculated using the energy balance equation as:

$$x = \sqrt{\frac{2E_{impact}}{K_{total}}} = 0.126\ m$$

The impact force transferred to the structure during the maximum deflection of the gear is:

$$F_{impact} = K_{total} \times x = 3.31\ KN$$

This is the maximum force that the system must safely absorb to maintain its structural integrity during impact.

3.3.13 Stresses on Landing Gear

Stresses are developed on the landing gear under various landing loads, including compressive, bending and torsional. At the worst case of landing, the drone lands on one leg with its full weight, whose stresses are calculated as:

F_N = 47.77 N, D_o = 16.2 mm, D_i = 15 mm

M_s = $F_N \cdot$ r = 47.77 x 0.155 = 7.4 Nm, y = 8.1 mm

Compressive stress is calculated using the following expression,

$$\sigma_p = \frac{F_N}{\frac{\pi}{4}(D_o{}^2 - D_i{}^2)} = 1.62\ MPa$$

Bending stress is calculated using the following expression,

$$\sigma_s = \frac{M_s \cdot y}{I} = \frac{M_s \cdot y}{\frac{\pi}{64}(D_o{}^4 - D_i{}^4)} = 66.9\ MPa$$

The principal stress of the leg is calculated using the following expression,

$$\sigma_{1/2} = \frac{\sigma_x - \sigma_y}{2} \pm \frac{1}{2}\sqrt{(\sigma_x - \sigma_y)^2 + 4 \cdot \tau_{xy}{}^2}$$

Substituting the known values in the above expression, we get

$\sigma_1 = 66.9\ MPa$

$\sigma_2 = -1.62\ MPa$

3.3.14 Pump and Nozzle Selection

A 12V DC pump with a flow rate of 2 L/min was selected for spraying pesticide, considering the capacity of the tank of 0.5L to ensure uniform coverage of about 0.05 ha (=500 m^2) with the application rate of 10L/ha. Considering a uniform spray pattern and low drift loss, a locally available adjustable cone-type nozzle with a diameter of 1.8 mm was selected. The selected spraying system satisfied the criteria of spray efficiency, manageable reaction forces and operational safety.

The jet velocity at the nozzle exit was determined from the volumetric flow rate (Mitchell, 2014) and the reaction n force developed on the drone was calculated using:

$$Reaction\ force\ (F) = \frac{4\rho Q^2}{\pi d^2}$$

Where,

density of liquid (ρ) = 1000 kg/m³

volumetric flow rate through two nozzles = 0.83L/min = 1.38×10^{-5} m³/s

volumetric flow rate per nozzle (Q) = 6.92×10^{-6}

nozzle diameter (d) = 1.mm = 1.8×10^{-4} m

For the selected nozzle and flow rate, the reaction force is:

$$F = \frac{4 \times 1000 \times (6.92 \times 10^{-6})^2}{\pi \times (1.8 \times 10^{-4})^2} = 0.019\ N$$

The moment about the center of gravity due to the nozzle reaction is:

$$\tau = F \times R$$

Where R is the horizontal distance from the CG to the nozzle i.e., 0.32m. Substituting the values:

τ =0.00608 N

These calculations confirm that the hexacopter can maintain stability during spraying while delivering the required coverage.

3.3.15 Battery Selection:

The drone requires a continuous power supply to meet the power requirements of the electronic components. The dynamic movements of the drone and pesticide sprayer system demand a high power requirement throughout the flight. The total flight time of the drone to deplete the pesticide tank is estimated as;

$$Time\ required\ to\ spray = \frac{tank\ capacity}{flow\ rate} = \frac{0.5}{0.83} = 0.602\ min$$

Time required to take off, reach the field/spray zone and return = 3 min (assumed)

Total flight time = 0.60 + 3 = 3.60 min

Current Requirement:

Current required = 6 × Current requirement for a single motor = 150 amp

Current requirement for Pixhawk 2.4.8 = 3Amp (peak)

Current requirement for pump = 0.5 Amp

Total current requirement = 150+3+0.5 = 153.5 Amp

∴ Battery Capacity (Ah) = Flight Time (hours) × Total Current Drawn (A) = 9.21 Ah

A 13Ah battery was selected with a C rating of 25 slightly higher than the calculated capacity to account for safety and efficiency losses.

3.3.16 Acceleration Calculation:

The theoretical acceleration that the drone can achieve was calculated using the equilibrium equation as;

$\Sigma F_x = \mathrm{m} \cdot \mathrm{a}$

$\mathrm{T} - \mathrm{W} = \mathrm{m} \cdot \mathrm{a}$

$17.266 \times 6 - 4.87 \times 10 = 4.87 \times \mathrm{a}$

$\mathrm{a} = 11.27\ \mathrm{m}/s^2$

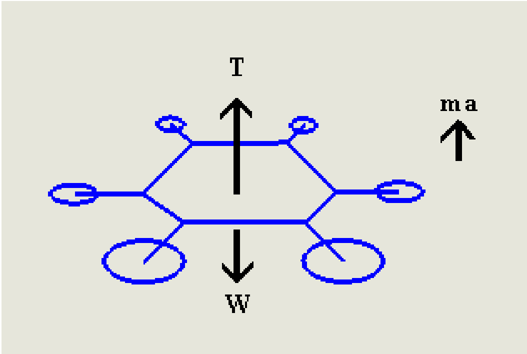

Figure 20: Free Body Diagram of the Drone

The drone can attain a maximum upward acceleration of 11.27 m/s^2 at full power and depicts that the drone possesses enough lift capacity to take off quickly and maneuver.

3.4 CAD Modelling

The complete structure of the drone was modeled and assembled in SolidWorks 2024. The general view of the assembled drone in SolidWorks is shown in figure 23.

Figure 21: Assembled Drone Model

3.5 Structural Simulation and Analysis

The 3D model of the hexacopter drone was prepared in SolidWorks after the design parameters were finalized and materials were selected. The geometry was imported to the ANSYS Workbench environment for static structural analysis. The thrust generated by each propeller and inertial forces and weights of different components were accounted in the structural analysis of the drone frame. Finite element discretization is performed by the ANSYS Mechanical solver and discretized elements are solved for the continuum mechanics equilibrium equations. The fundamental governing equation implied by the FEM solver is

$$[K].\ [u] = [F]$$

Where K is the stiffness matrix of elements

u is the nodal displacement matrix

F is the nodal forces

Static structural analysis of the drone frame follows the following procedures.

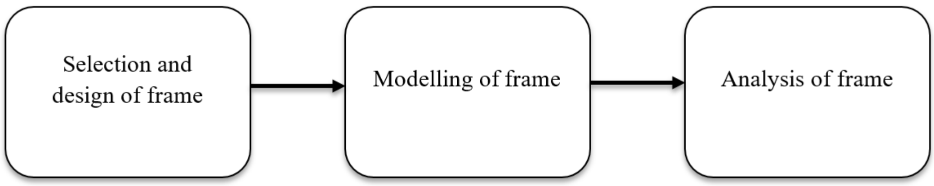

Figure 22: Methodology of static analysis of the drone frame

Materials were assigned to the drone parts in ANSYS Mechanical. 6063 T5 anodized material was assigned to the arms and aluminum alloy material to the base and top plates. The boundary condition applied to the geometry mimicked that of the physical model. All six DOFs of the frame had to be avoided to prevent the rigid body motion; the geometry was constrained in three insignificant locations of the battery mount, having one fixed support and two displacements constrained in the x and y directions simultaneously. The inertial relief feature was turned on to mimic a hover flight state of the drone frame as it automatically balances the applied loads with generated translational and rotational acceleration. The external resultant forces are calculated to add the internal inertial forces internally, which balances the structure and $\sum$forces =0 and $\sum$moments = 0, allowing the frame to deform naturally without artificial supports.

The thrust force of 18N, a little higher than the calculated thrust due to each motor and propeller, was assigned to the individual arms of the Hexacopter. Standard earth gravity was assigned to the center of gravity of the drone frame and a remote force of 21N representing the inertial mass of the battery and payload was applied to the base of the drone frame. The analysis setup is shown in the figure below:

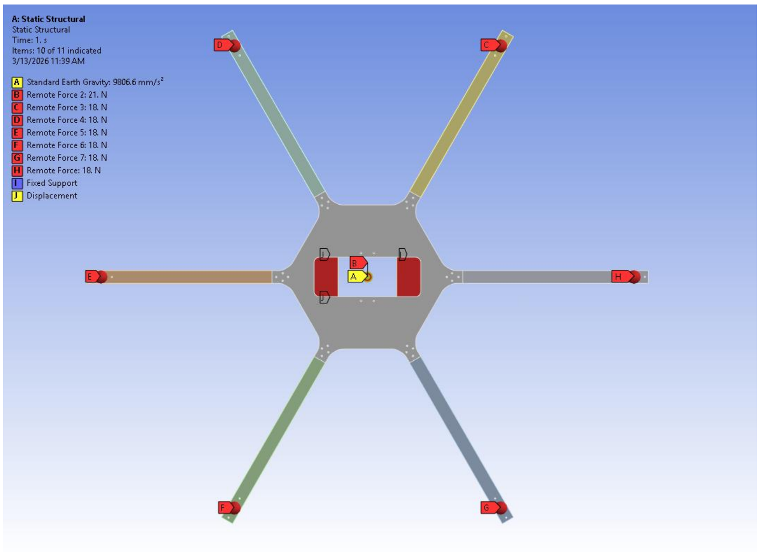

Figure 23: Boundary Conditions on Initial Structure

Below are the tables comprising material properties assigned to different parts of the drone frame for structural analysis.

Material Properties of AL 6063-T5 Anodized Aluminum

Properties	Value	Unit
Density	2700	kg/m³
Young's Modulus	6.89 × 10^10	Pa
Poisson's Ratio	0.33	-
Bulk Modulus	6.7549 × 10^10	Pa
Shear Modulus	2.5902 × 10^10	Pa
Tensile Ultimate Strength	1.86 × 10^8	Pa
Tensile Yield Strength	1.45 × 10^8	Pa
Thermal Conductivity	210	W/m·°C

Table 14: Material Properties of AL 6063-T5 Anodized Aluminum

Material Properties of Aluminum Alloy (General)

Properties	Value	Unit
Density	2770	kg/m³
Young's Modulus	7.1 × 10^10	Pa
Poisson's Ratio	0.33	-
Bulk Modulus	6.9608 × 10^10	Pa
Shear Modulus	2.6692 × 10^10	Pa
Tensile Ultimate Strength	3.1 × 10^8	Pa
Tensile Yield Strength	2.8× 10^8	Pa
Thermal Conductivity	167	W/m·°C

Table 15: Material Properties of Aluminium 6061 Aluminium Alloy

The joints between the arms and the center plates of the drone frame had been modeled with bonded contacts, which acted as a glued or a welded joint. Non-conformal mesh was generated between the mating surfaces to avoid a higher computational cost, yet considerable results were obtained through contact modeling. The continuity of displacement of nodes between the interfaces is enforced by the bonded contact

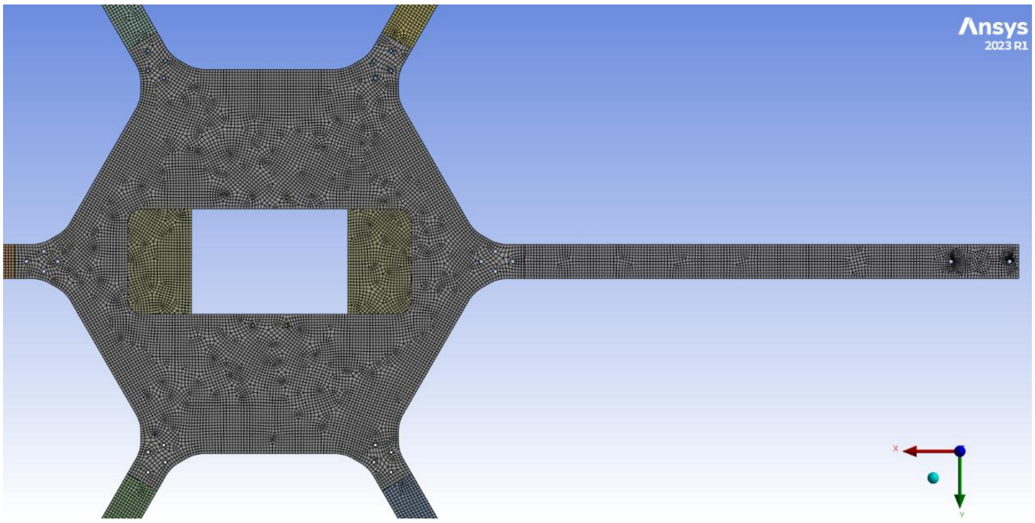

Figure 24: Mesh Generated in the Initial Design

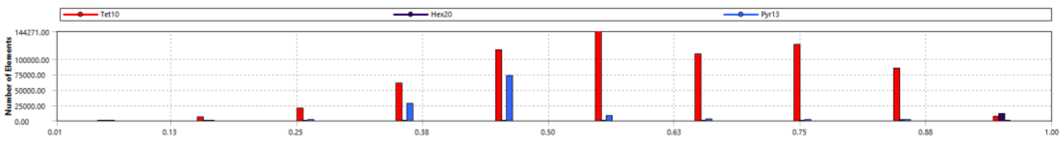

Figure 25: Element Quality of Initial Design

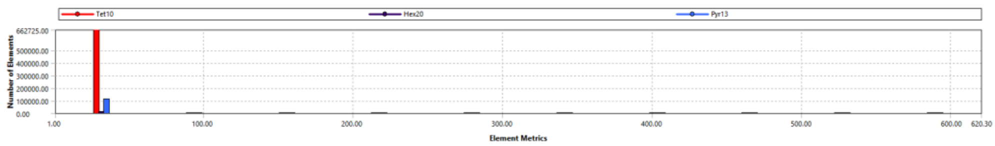

Figure 26: Aspect Ratio of Initial Design

. The drone frame was meshed using a multi-zone meshing method to create a structured and mapped mesh, which is computationally efficient compared to unstructured meshes. Most parts of the mesh consisted of hexahedral elements, while a few locations consisted of tetrahedral and prism meshes as a free mesh type responsible for generating a fine mesh. Local sizing controls were added to the critical regions and different parts of the drone frame and generated a total of 787836 elements in the initial frame design. The frame was meshed with a target to maintain a minimum element quality of 0.13. Then, the mathematical model was solved to calculate the total deformation and equivalent stress distribution in the drone frame.

This analysis of stress distribution helped us further in the topology optimization of the drone frame and reduce unwanted weight from the drone frame. The minimum stressed zones of the drone frame were considered for material removal. After considering the areas of material removal, the final design was remodeled in SolidWorks and imported to ANSYS workbench for design validation. All boundary conditions were imposed as of the initial design and all meshing parameters followed that of the initial design. The final mesh consisted of 824553 elements and were targeted to maintain a minimum element quality of 0.13. The final mathematical model was solved for total deformation and stress development.

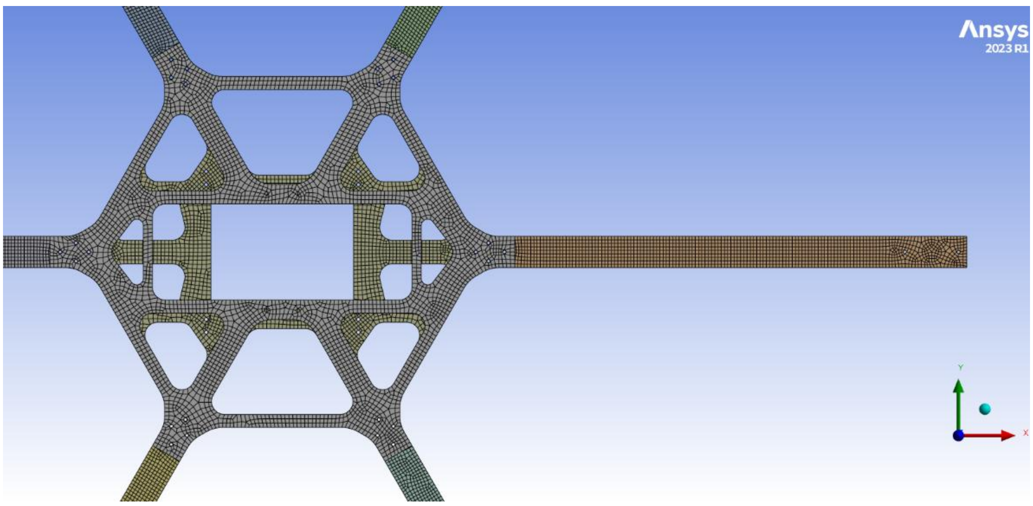

Figure 27: Mesh Generated on the Final Design

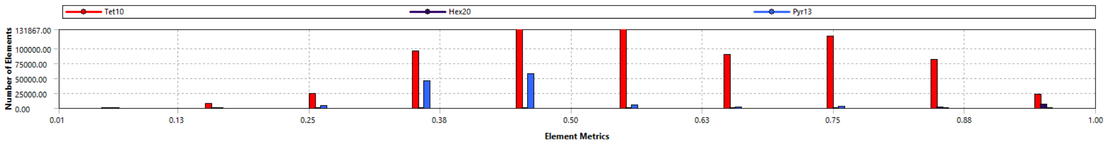

Figure 28: Element Quality of Final Design

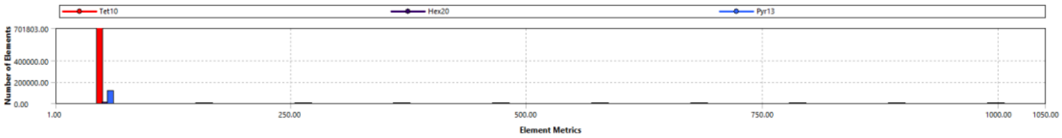

Figure 29: Aspect Ratio of Final Design

3.6 CFD Analysis of a 15x5.5 Propeller in ANSYS Fluent

The selected propeller of diameter 15 inches with a pitch of 5.5 inches was simulated with the finite volume solver in ANSYS Fluent for propeller thrust and flow field analysis. A series of computational fluid dynamics simulations was carried out in the ANSYS Workbench 2023 R1 environment. The Reynolds-Averaged Navier-Stokes (RANS) equations were used to model and govern the flow field as a steady-state, incompressible turbulent flow based on time-averaged equations. The finite volume method FVM discretizes a spatial volume into several finite volumes called cells, each possessing a non-overlapping property and connected through faces to each other. Initially, the partial differential equations are integrated for each control volume, which is later transformed into algebraic equations, as it is easier to solve. The governing equations consist of the conservation of mass and momentum.

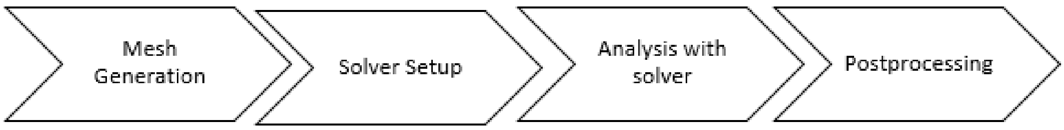

Figure 30: CFD Methodology

3.6.1 Continuity equation:

$$\nabla \cdot \vec{\vec{V}} = 0$$

Where, $\vec{\vec{V}}$ = mean (time-averaged) velocity vector

It describes a mass conservation equation for steady flow where the divergence of velocity vector equals zero (Alfonsi, 2009). This means that the fluid entering a control volume equals to the fluid leaving it and no mass is created in between.

3.6.2 Conservation of momentum

$$\rho\left[\frac{\partial\vec{\vec{V}}}{\partial t} + \vec{\vec{V}}\,.\nabla\,\vec{\vec{V}}\right] + \rho\frac{\partial}{\partial x_j}\left(\overline{u_i{}'u_j{}'}\right) = -\nabla\bar{p} + \mu\nabla^2\,\vec{\vec{V}}$$

ρ = Fluid Density

p̄ = Mean Pressure

μ = Dynamic Viscosity

$\overline{u_i{}'u_j{}'}$ = Velocity fluctuations (Reynolds Stresses)

This equation describes the conservation of momentum in time-averaged turbulent flows (Alfonsi, 2009). The term $\rho\left[\frac{\partial\vec{\vec{V}}}{\partial t} + \vec{\vec{V}}\,.\nabla\,\vec{\vec{V}}\right]$ represents transient and convective acceleration of the mean flow, while the term $\rho\frac{\partial}{\partial x_j}\left(\overline{u_i{}'u_j{}'}\right)$ represents turbulent momentum transport. The right-hand side terms represent the pressure forces and viscous diffusion.

3.6.3 Geometry Preparation and Mesh

The propeller was initially modeled in SolidWorks and the computational domains required for the analysis of the propeller was modeled in ANSYS SpaceClaim, consisting of two domains viz. rotary domain and the stationary domain.

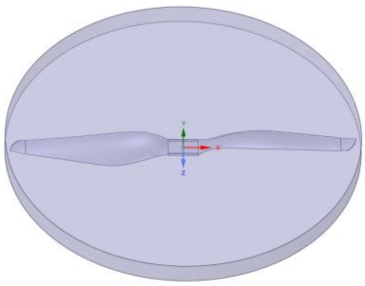

Figure 31: Rotary Domain

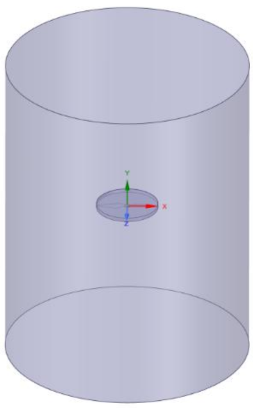

Figure 32: Stationary Domain

The rotary domain is a cylindrical flow enclosure consisting of the propeller. The stationary domain, having dimensions of radius 690.5mm and a total height of 1008 mm, represents the surrounding fluid region and is sufficient to allow proper downstream wake development.

Since the geometry is symmetric, only half of the full configuration was simulated to reduce the computational cost and time. To apply the periodic boundary condition, the rotary domain was split into two lateral surfaces to represent the repeating flow pattern, which significantly reduced the number of cells and preserved essential aerodynamic characteristics of the propeller. Finally, the topology of geometries was shared for the creation of a conformal mesh, which would lead to accurate solutions for a CFD mesh.

A watertight geometry workflow of the ANSYS Fluent was used to mesh the computational domain, as it simplifies the process of mesh generation and is also capable of high-quality mesh generation. Local sizing controls were utilized in the rotary domain to refine the mesh and inflation layers were added to the boundary regions.

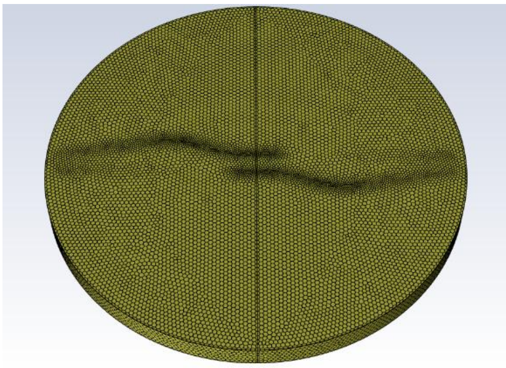

Figure 33: Mesh Generated at the Symmetric Rotary Domain

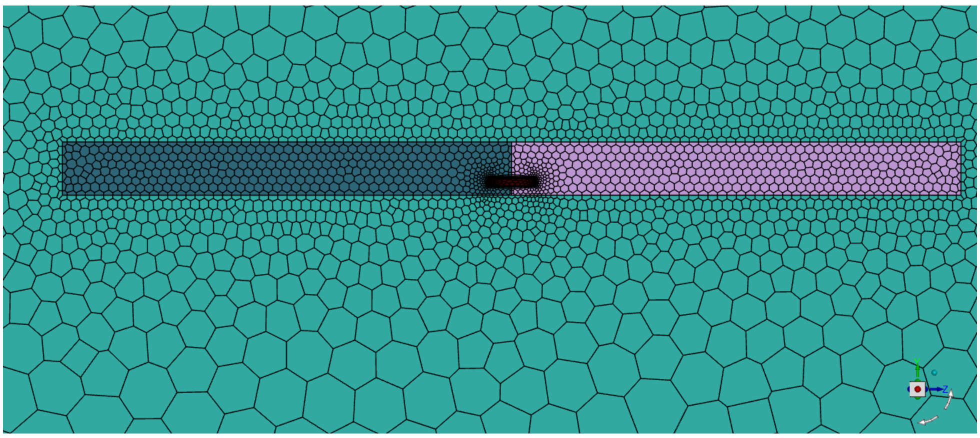

Figure 34: Mesh Generated at Periodic Boundaries

The polyhedral mesh generated with this approach possessed a minimum orthogonal quality of 0.16 and a maximum aspect ratio of 136.559. The total cell count of the final simulation after a series of grid independence tests numbered 174092. Five boundary layers were added in the fluid region near the propeller blade surface, with the first layer thickness of 4×10^{-5} m and a growth rate of 0.272 to maintain the required y+ value equal to 1. The first layer thickness is provided by the following equation (Fejes, 2024).

$$y = \frac{y^{+}\upsilon}{\rho u_{\tau}}$$

where, υ is kinematic viscosity and

u_{τ} is the friction velocity

The stress tensor developed in the RANS equation has to be accounted with a turbulence model. Thus, a two-equation (Shear Stress Transport) SST k – omega turbulence model was employed to solve the computational mesh as it accounts for both the change in pressure gradients and flow separation and is widely used in turbomachinery simulations. It combines the advantages of both the k-ε model in the free stream and the k-ω model in near wall region.

Wall Boundary Condition	
Propeller	Wall
Wall Motion	Stationary Wall
Shear Boundary Condition	No slip
Outlet Boundary Condition	
Outlet Type	Pressure Outlet
Gauge Pressure	0 MPa
Periodic Boundary Condition	
Periodic 1	Periodic
Periodic 2	Shadow
Symmetry Boundary Condition	
Symmetry Plane	Symmetry
Properties of Flowing Fluid	
Fluid	Air
Density	1.225 kg/m3

Table 16: Boundary Conditions for Propeller CFD

The Multiple Reference Frame (MRF) approach was utilized to model the propeller motion to avoid the higher computational costs of transient sliding mesh techniques and solve governing equations with a rotating coordinate system. The rotational speed of the propeller was assigned at 8500 rev/min based on theoretical calculations. The governing equations were discretized using pressure based solver using Finite Volume Method and the PRESTO scheme was utilized to interpolate pressure suitable for rotating flows. Green-Gauss node-based method was utilized to compute velocity gradients with gradient accuracy, while variables like momentum, turbulent kinetic energy and specific dissipation rate are assigned with the QUICK scheme.

Three outer surfaces of the stationary domain are assigned pressure outlet and equally divided lateral surfaces of the rotary domain are assigned for periodic boundary conditions. The plane cutting the stationary domain into equal halves is assigned a symmetric boundary condition. There is no inlet boundary condition as the flow is generated itself using the MRF approach, as the rotating blades impart momentum to the stationary fluid. The residuals were set to converge at 1×10^{-4} and the computation was initialized with a relaxation pressure factor of 0.5.

3.7 Control system and drone controls

Pixhawk 2.4.8 controls the overall performance of the drone anticipating the provided radio frequency as well as PID controls. TX protocol of communication is established between the FS-i6 transmitter a FS-iA 10B receiver while RX protocol is established between the receiver and the flight controller. The transmitter uses 2.4GHz AFHDS 2A (Automatic Frequency Hopping Digital System) protocol with GFSk (Gaussian Frequency Shift Keying) modulation to avoid interference between transmitters. The radio receiver receives PPM (Pulse Position Modulation) protocol in this case combining signals of all channels into a single one. The four channels of the transmitter transmit signals to maneuver drone in roll, pitch, throttle and yaw axes. Additional two channels work as switch to change the flight modes and operate the pump. The control system in Pixhawk analyzes the signals from the radio transmitter and the sensors onboard viz. GPS, gyroscope, accelerometer and barometer. The system evaluates the error in the system and minimizes it through PID loop.

The hardware components of Pixhawk 2.4.8 (FMUv2) flight controller are as follows:

i. System-On-Chip STMicroelectronics STM32F427 Cortex-M4F 32-bit main microcontroller, operating frequency 180 MHz, RAM: 256 KB SRAM (L1), 2 MB Flash memory for writing instructions.

ii. System-On-Chip STMicroelectronics STM32F100 Cortex-M3 32-bit, 24 MHz operating frequency, 8 KB SRAM (L1), 64 KB Flash memory for writing instructions.

Embedded sensors on the motherboard:

i. a 3-axis STMicroelectronics L3GD20H 16-bit gyroscope sensor;
ii. a 14-bit STMicroelectronics LSM303D accelerometer/magnetometer sensor;
iii. an Invensense MPU-6000 3-axis accelerometer/gyroscope sensor;
iv. a TE Connectivity MEAS MS5611 barometer sensor.

The PID loop of the flight controller translates the stick inputs to command ESCs and maintain stability of the drone. The controller continuously calculates an error i.e. the difference between where the drone should be (Set point) and where it actually is (measured by gyros and sensors). It then uses three terms to correct this error.

i. Proportional gain (K_P): It minimizes the tracking error and is responsible for a quick response. It is set as high as possible without introducing oscillations to it. Higher value of P gain introduces high-frequency oscillations in the system whereas its lower value makes the system react slowly to input change.
ii. Integral gain (K_I): It accumulates the error over time that occurs due to external factors like wind or off-center weight.
iii. Derivative gain (K_D): It predicts future error analyzing the rate of change and is set only as high as needed to avoid overshoots.

The general form of the PID controller is given below:

Error signal:

$$e(t) = x_d(t) - x(t)$$

PID control law:

$$u(t) = K_P e(t) + K_I \int_0^t e(t)\ ds + K_D \frac{de(t)}{dt}$$

where u(t) is the control input and e(t) represents the error function between the desired position $x_d(t)$ and the actual state x(t). The coefficients K_P, K_I and K_D represent the parameters for the proportional, integrative and derivative components of the PID controller. The general scheme of closed loop PID controller is shown in Figure 36.

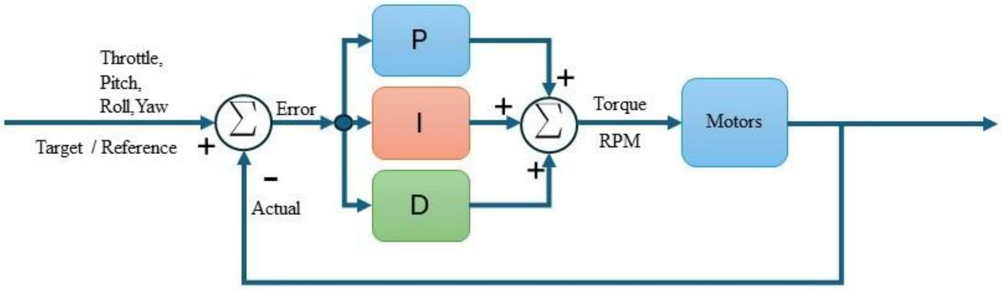

Figure 35: PID Control Scheme

The sufficient value of the throttle lifts up the drone and stabilizes its attitude. With continuous input from the transmitter, the drone reaches the desired altitude, with corrections made by the PID controller. The PID receives signals from the onboard IMU sensors to maintain stability, applying corrections to the errors. The correction signals are then fed to the ESCs to control the speed of the rotors and stabilize the drone.

The drone can be maneuvered in different flight modes, viz. Stabilize, Alt hold, RTL, Land and Loiter. The flight modes utilized in the drone system are explained below:

i. Stabilize: The PID controller adjusts pitch and roll by itself and hence requires no full control from the operator.
ii. Loiter: This mode is applied during semi-autonomous flights where PID controllers maintain altitude and position while GPS is used to hold the drone's location.
iii. Land mode: The hexacopter descends and lands vertically without returning to the take-off point.

The system utilizes Loiter mode instead of Alt Hold as it provides maximum stabilization in the flight due to use of GPS for position control. All three modes were used during the testing phase to observe the stability and performance of the drone. Fixed point test was performed to observe position drift, altitude stability and controller response.

3.7.1 Pixhawk Configuration

An open source Ardupilot firmware based on mission planner software is used to configure Pixhawk for the hexacoter. A laptop is acts as the ground control station with the mission planner platform installed. Firmware is installed through the mission planner software to the motherboard of the Pixhawk using a USB Type-B cable. Hex-X configuration was selected during the initial setup followed by hardware calibrations.

The GPS module and Pixhawk flight controller were attached intact to the drone structure preventing position change after calibration. Under the mandatory hardware setup, calibration of the accelerometer was done involving the positioning of drone in six different extreme positions of maneuver, viz. left, right, nose-down, nose-up and back. This followed the calibration of compasses present on both the GPS and Pixhawk for successful calibration of accelerometers and was concluded with movements made at different axes in 3D space. The radio was calibrated moving joysticks and toggle switches to extreme positions, finally leading to the calibration of ESCs. Channel five was assigned for toggle switch (SwC) to assign stabilize, loiter and land flight modes. The fail safe option was enabled and set to trigger at a low voltage of 13.2V to safely land the drone using RTL mode.

3.8 Fabrication of Hexacopter Drone

Figure 36: Fabricated Pesticide Spraying Hexacopter

The structure of the drone was fabricated with Aluminium alloy material. The arms of Aluminium 6063 material were machined at a dimension of 500mm x 24mm x 1mm. The plates of Aluminium 6061 material, having dimensions 400mm x 400mm x 3mm, were machined via CNC Laser. The arms and base plates were fastened with M3 nut bolts. The drawings of the base plate and the upper plate are shown in Figures 39 and 40 respectively.

3.8.1 Tank Design and Fabrication

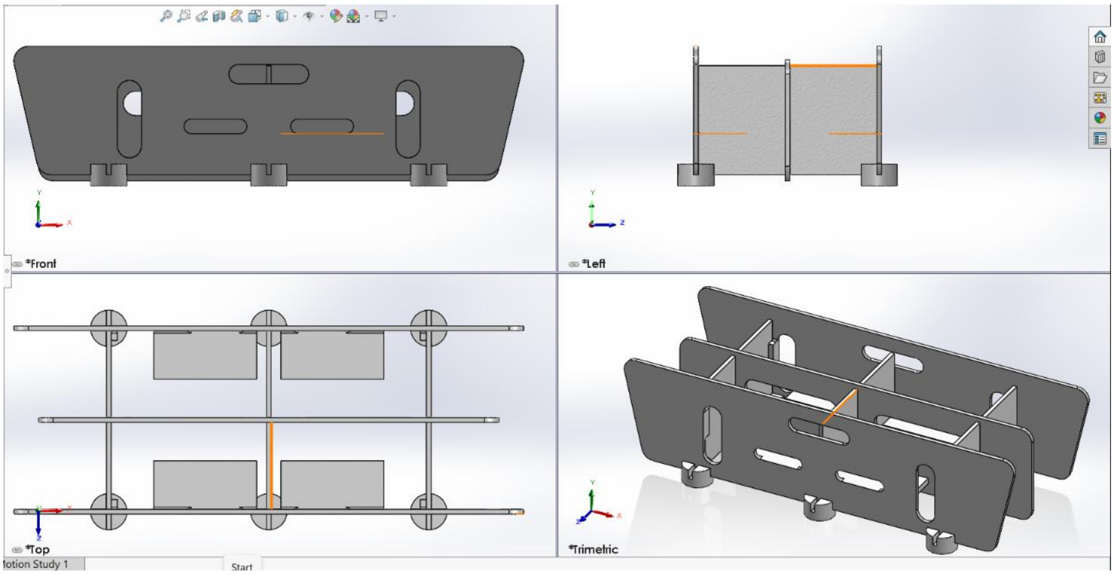

Figure 37: Tank Baffle Design

The tank was incorporated with a vertical grid-like system of baffles to minimize the turbulence generated by liquid waves. This restricts the flow of liquid over small volumes, aiding to the stability of the drone flight.

3.9 PID Tuning of Drone

The fabricated model was initially tuned for PID parameters on the setup shown in Figure 42. Each arm was constrained with a rope length 0.7m to restrict the flight of the drone within this altitude. Changes in values of proportional, integral and derivatives were made to observe their effect on the stability of the drone.

3.10 Thrust Test

The thrust generated by the propulsion system was measured using a thrust-test setup. The motor was mounted on the bottom of a digital spring balance suspended vertically. Thrust at different values of the throttle and current input were observed and plotted.

3.11 Spray Tests Incurred

The custom built spraying system from locally available nozzle and pipe was assessed for its performance through different tests. The specifications of the drone mounted sprayer system is presented on table 17.

Parameters	Value
Pump Discharge	2 l/ m
Nozzle Type	Swirling nozzle
Number of Nozzles	2
Nozzle spacing	61cm
Tank Capacity	1L
Sprayer Discharge	0.83 l/min

Table 17: Specifications of Sprayer System

3.11.1 Discharge rate

The discharge rate was measured at the operating pressure of the pump at 14.8V. Two measuring cylinders were placed below the nozzles to calculate the volume of the sprayed liquid.

Discharge = volume/time

3.11.2 Spray Uniformity

The drone-mounted sprayer was operated at five different heights above the custom-designed patternator to measure the spray uniformity. The height was varied from 800mm to 1600mm with an interval of 200mm. A patternator with 31 channels was designed using corrugated roof panels having dimensions of 2134mm x 2500mm and was inclined at an angle of 12 degrees. The patternator setup shown in Figure 44 was used to measure swath width, spray uniformity and spray liquid loss. The liquid was collected in each vessel attached to individual channels and later measured using measuring cylinders.

3.11.3 Spray Liquid Loss

Spray liquid loss is mainly accrued due to the wind velocity and atomization of liquid droplets. The spray loss was calculated at a flight height of about 1-2m above the surface of the patternator and measuring the difference between the sprayed volume and collected volume.

3.11.4 Droplet size and density

The spray was colored with laundry blue and droplets were cast upon the photographic paper. The paper was dried for 24 hours and the diameter of droplets were analyzed and measured. Altogether 8 papers were placed in the ground and arranged in two columns, with 3 papers in each column with a distancing of 1m between them ensuring uniform sampling across the swath width. 2 papers were placed in between the columns equidistant from surrounding 4 papers. The drone was hovered at a height of about 1-2m above the papers to have them sprayed. The samples were collected, scanned and analyzed for spray deposition using image J software.

CHAPTER 4: RESULTS

4.1 Static Structural Analysis of Initial Design

The total deformation and equivalent stress contours were obtained after the solution of mathematical models. Element size was reduced to obtain better values of element quality and equivalent stresses, resulting in a mesh independence study for the structural analysis of the drone frame. The simulation provided us with an equivalent von Mises stress of 12.961MPa and a total deformation of 0.51813mm after the final iteration. The stress distribution, deformation of the drone frame and stress convergence graph of the grid independence study are shown in the figures below.

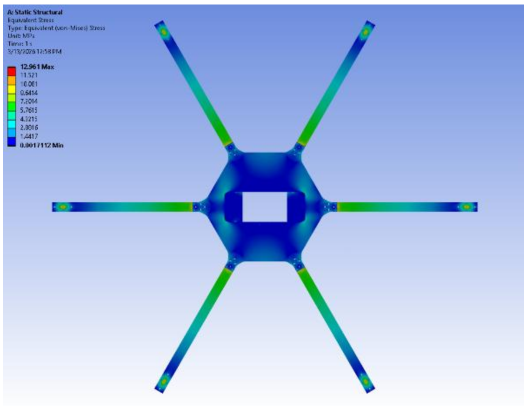

Figure 38: Equivalent Stress Contours on Initial Design

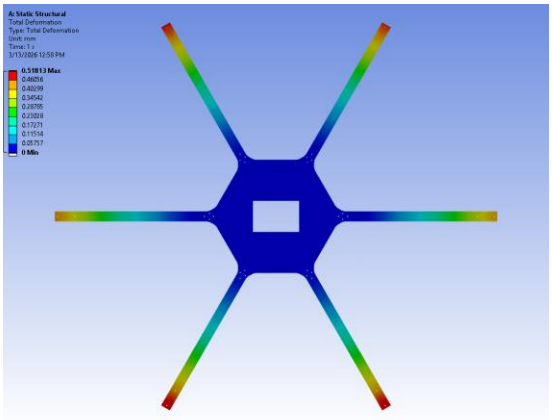

Figure 39: Deformation Contours on Initial Design

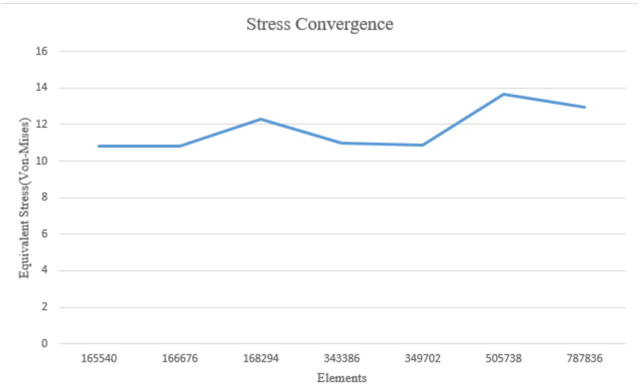

Figure 40: Mesh Independence Study on Initial Design

4.2 Static Structural Analysis of Final Design

A mesh independence study of the final design was performed to obtain a reliable value of equivalent stress and total deformation. The equivalent (Von-Mises) stress resulted in a value of 14.772MPa and the total deformation resulted in 0.73042mm. The stress distribution, total deformation on the final design and stress convergence graph of the mesh independence study are depicted in figures 41, 42 and 43 respectively.

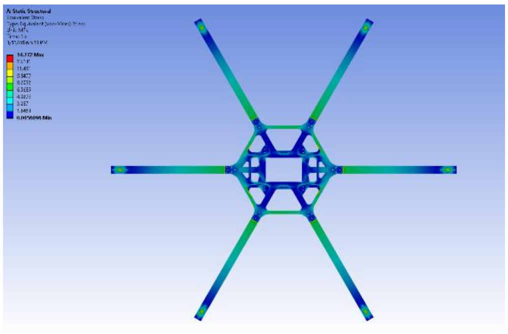

Figure 41: Equivalent Stress Contours on Final Design

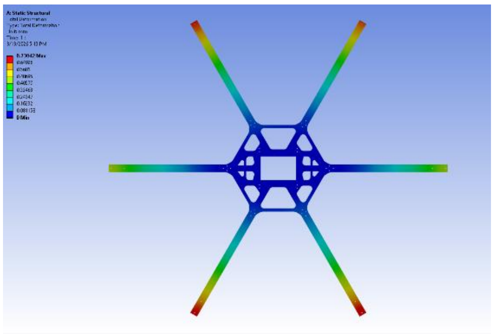

Figure 42: Total Deformation Contours on Final Design

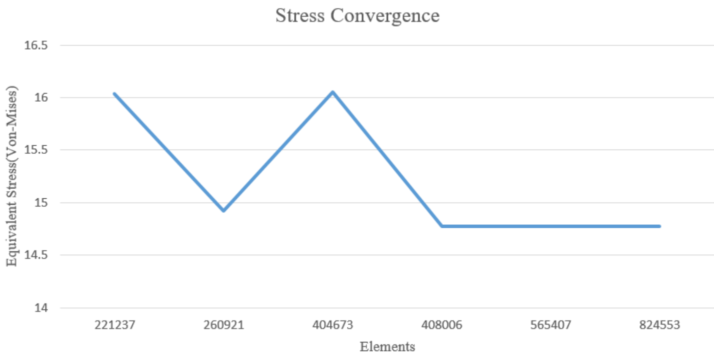

Figure 43: Mesh Independence Study on Final Design

4.3 CFD analysis of a propeller

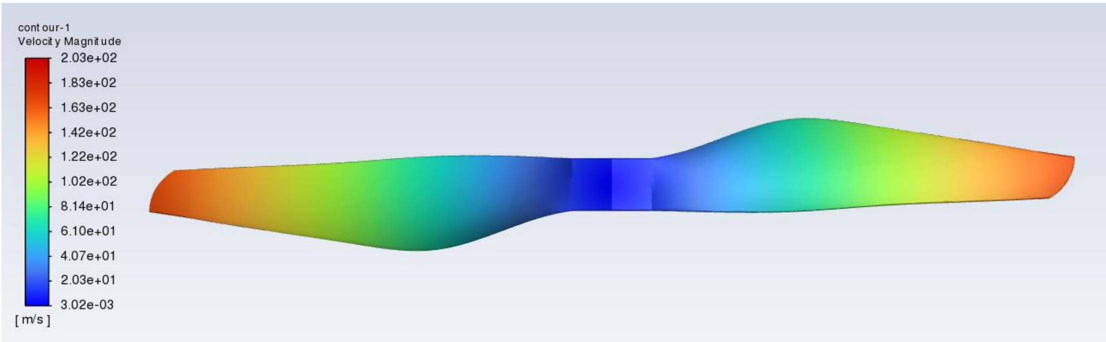

Figure 44: Periodic Instancing of Propeller Velocity Contours

The computational domain was solved for different numbers of cells to perform a mesh independence study and to observe the change in propeller thrust with increasing number of cells. The solution of the domain converged at 446 iterations, generating a thrust force of 12.9167N after a series of grid independence tests. The following are the convergence of propeller thrust, velocity and pressure contours of the 15x5.5 Propeller.

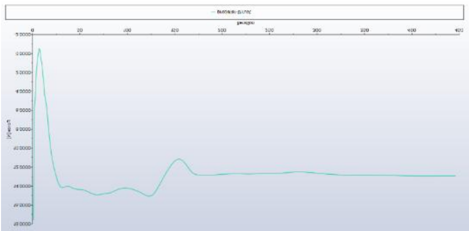

Figure 45: Propeller Thrust Force Graph

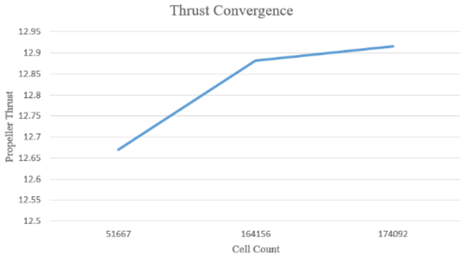

Figure 46: Mesh Independence Study on Propeller Thrust

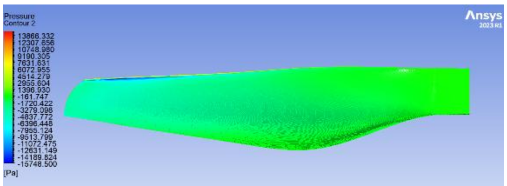

Figure 47: Pressure Contours on Propeller

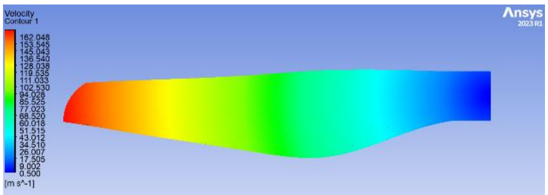

Figure 48: Velocity Contours on 15x5.5 Propellers

4.4 Thrust Test of the Propeller

The thrust test on the propeller was conducted on the setup varying throttle of the transmitter which consequently varies the current input. The graph shown in Figure 49 depicts that the thrust increases almost linearly with increase in current. Thrust vs Current graph displays a steep rise at the range of 0-6A and slowly flattens at the range of 6-25A due to environmental and instrumental losses. Figure 57 highlights the differences between theoretical and experimental values with a maximum of 1350 gm measured thrust.

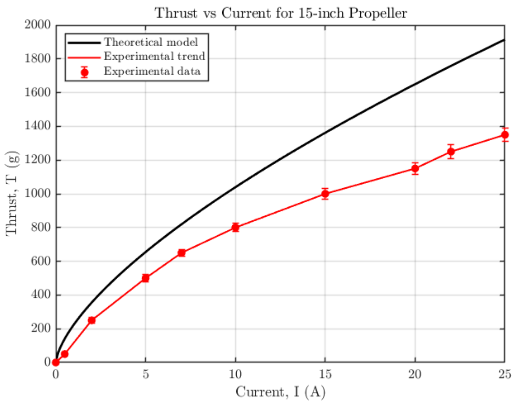

Figure 49: Thrust vs Current Graph

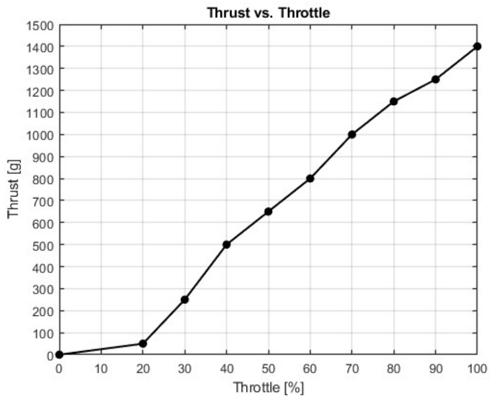

Figure 50: Thrust vs Throttle Graph

The thrust vs throttle graph shown at Figure 50 depicts a slight increase in thrust from 0 to 50 gm as the throttle rises from 0% to 20%. This zone represents a dead zone with high power consumption to overcome the static friction of the motors and provide starting torque to the rotors. The throttle range of 20-80% show steep rise in thrust and slowly flattens in the range of 80-100%, suggesting the motor becomes less efficient at higher throttle with higher power consumption.

4.5 Swath Width and Spray Uniformity Test

The static test result of the spray mechanism having a lance length of 61cm for flow distribution and swath width is shown in Figure 51. The graph depicts a normal distribution of the flow. The central channels have the maximum volume as compared extreme channels. The flow distribution graph depicts that the swath width increased from 1550mm to 2400mm as the height of the spray increased from 800mm to 1600mm. The swath width was measured using a measuring tape over the wet channels. The test result showed uniform distribution of spray at a height range of 1.4m-1.6m with the mean flow distribution of nearly 30m^3/s.

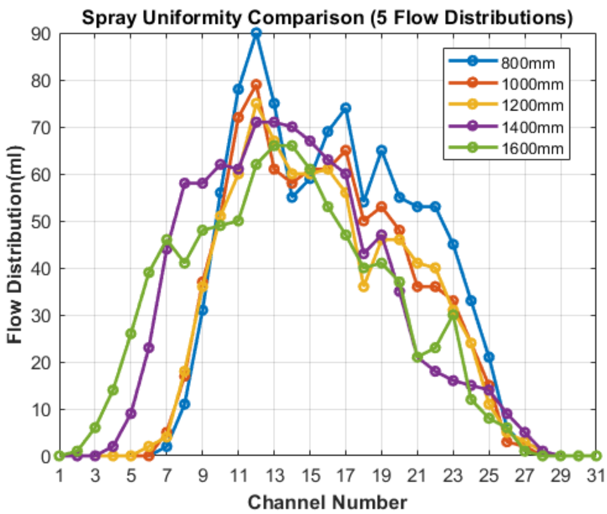

Figure 51: Flow Uniformity Over Patternator Channels

S.N.	Spray Height(mm)	Swath width(mm)	Peak flow(m^3/s)	Mean flow (m^3/s)	Coefficient of variation
1	800	1550	90	31.61	95.16%
2	1000	1960	79	27.94	93.74%
3	1200	2100	75	25.42	97.21%
4	1400	2200	71	30.42	84.78%
5	1600	2400	66	28.84	79.35%

Table 18: Summary Table of Spray Data

The Table 18 shows the swath width, peak flow, mean flow and coefficient of variation of flow distribution corresponding to different spray heights. The coefficient of variation measures the liquid distribution uniformity, with a variation observed to vary from 95.16% at 800mm spray height to 79.35% at 1600mm. The flow distribution at

1600mm is found to be the most uniform, suggesting a flight altitude of 1.6m above crops for the drone during spraying purposes.

4.6 Spray Loss Test

The spray liquid loss was measured on the patternator using a sample volume of 100 ml, with five successive tests yielding an average spray liquid loss of 25%.

Figure 52: Spray Liquid on Measuring Cylinder

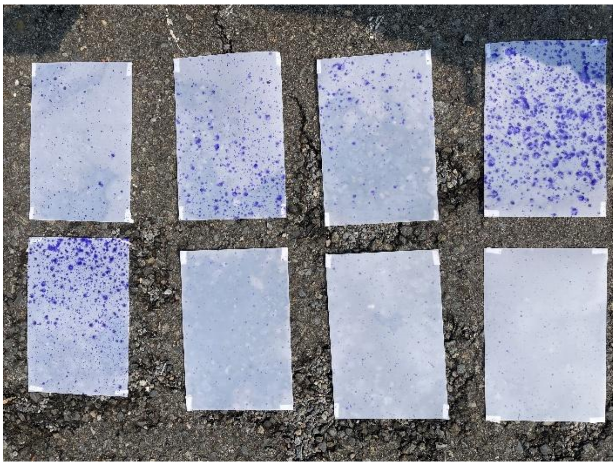

Figure 53: Sample Specimen of Droplets

4.7 Droplet Size and Density

The droplets were collected on photographic papers as shown in Figure 53. All the sample pieces were measured for the total number of droplets falling under the A4-sized paper during the hovering condition and movement. Among the range of 800-900 droplets per sample, 200 droplets of each sample were analyzed from the five different samples collected. The highest droplet density and coverage were observed on central papers directly beneath the hovering drone. The peripheral papers showed lower deposition showcasing non-uniform pattern across different samples.

Sample no.	Min area(mm^2)	Max area(mm^2)	Standard Deviation(SD)	Average area(mm^2)
1	0.002	115.053	1.962	12.576
2	0.058	63.455	11.291	9.607
3	1.157	45.31	8.144	9.17
4	0.060	49.428	8.680	8.232
5	0.124	59.242	8.173	5.593

Table 19: Spray Deposition Table

4.8 Flight Test

Flight data of the fabricated drone was analyzed for its stability, maneuverability and efficiency. The log file of the first flight data without payload was analyzed for the flight setup with parameters given in the table:

Parameters	No Payload (No Attachments)	With Payload (200 gm)
Take-off weight	3624 gm	4570 gm
GPS Mode	Loiter	Loiter
Altitude	2.82 m	2.75 m
Time	1min	1 min

Table 20: Flight Test Parameters

i. No Payload Flight Test

The throttle graph of the flight data was analyzed, plotting throttle PWM and time. It can be observed that about 65% throttle was used to lift the drone to a height of 2.82m. The PWM signals of six different motors were plotted and analyzed, which showed a maximum variation of 18%. The maximum PWM required for the six motors to hover was below 70% range.

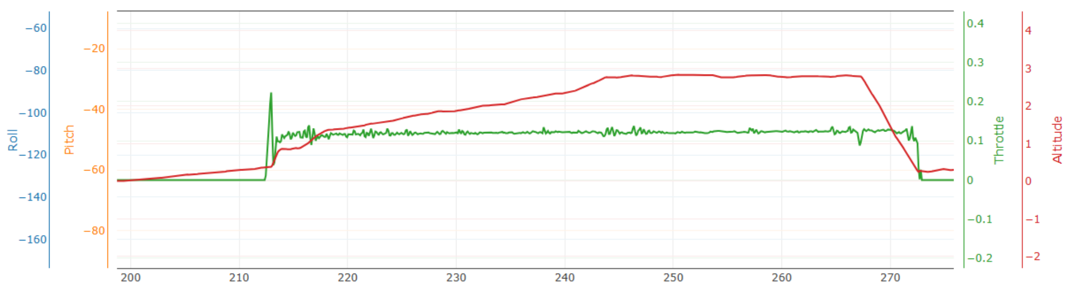

Figure 54: Altitude Coverage vs Throttle at no Payload

The correct design and assembly of the drone must possess as little vibration as possible, affecting the overall stability of the drone. The vibration parameter of the drone was measured by the accelerometer present on the flight controller. The observed vibrations in the drone frame were below the 15m/s2 mark, which portrays a good stability of the drone.

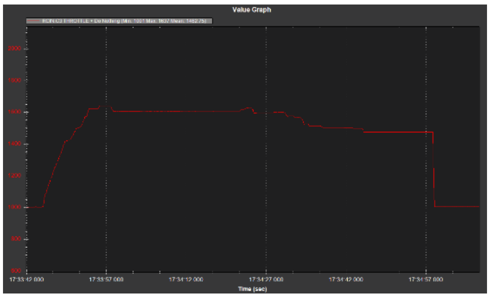

Figure 55: Throttle PWM Signals

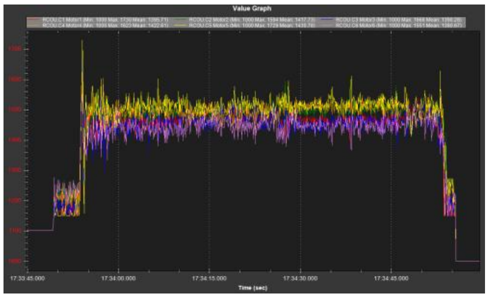

Figure 56:PWM Signals of Six Motors

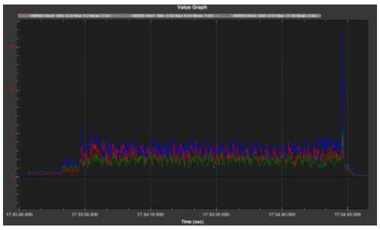

Figure 57: Vibration Levels of No Payload Flight

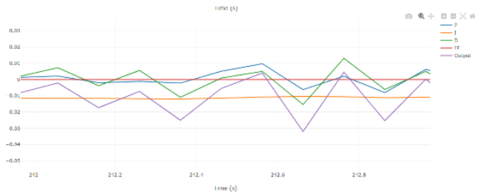

Figure 58: PID Graph of No Payload Flight

The PID graph shows no major oscillations, which depict a well-tuned drone and the flat integral displays no accumulation of a steady-state error. The nature of the proportional shows that it is continuously responsive to the increasing current and real-time variations. The integral is responsible to correct slight imbalances in the drone. The derivative component is responsible for damping and stability of the drone, preventing its overshoot. The graph of derivative terms displays sharp fluctuations, constantly stabilizing the drone against aerodynamic effects and structural vibrations.

ii. Flight test with a payload of 200ml

The hover flight test was conducted with a payload of 200ml in an open ground with an accuracy of 2-2.5m in Loiter flight mode. The drone was hovered at an average altitude of 2.75 for about a minute. The throttle vs altitude plot shown in Figure 59 was analyzed and found that the maximum height attained was 2.82m with the maximum throttle value of 0.27.

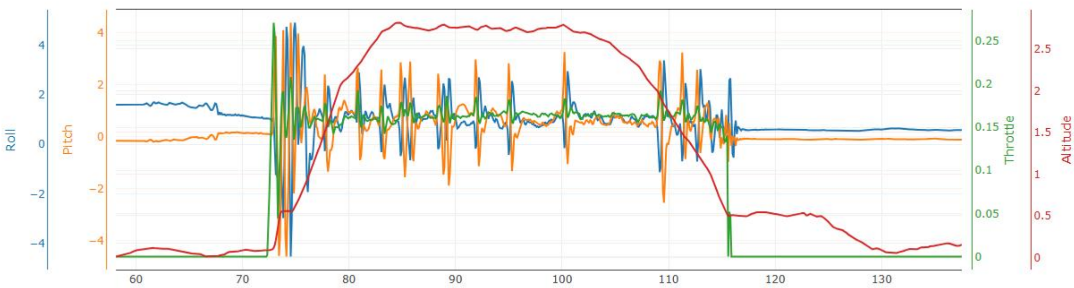

Figure 59: throttle vs Altitude of Payload Flight

The desired and actual altitude was plotted in a graph as shown in Figure 60 which depicts a very small variation of 0.04m, indicating a precise and robust altitude tracking capability of the drone suitable for precision agriculture. (Smith et al., 2020) found UAV altitude variation less than 0.5m acceptable for precision agriculture applications.

The throttle signals transmitted through the channel 3 of the transmitter is shown in Figure 61. The graph shows the signal transmitted with the maximum PPM of 1666, representing 63.3% of the maximum allowable PPM.

The throttle output curve and hover throttle is plotted with respect to time as shown in Figure 62. This is the actual throttle processed by the controller to maintain the desired altitude which shows that the throttle varied throughout the flight although the PWM signal provided was constant due to PID control. The mean throttle evaluated by controller for the drone to hover was 0.16.

The PWM signals of the transmitter from 5 different channels are plotted as shown in Figure 63. The graph shows the strength of PWM signals provided to each channel and how the controller processed it to maintain the stability during the flight. The graph shows no change in roll and pitch displaying a constant strength of 1500 while the yaw varied between 999 and 1500 PWM. The graph shows the flight of in loiter mode corresponding to the signal of 1500.

The motor PWM signal graph shown in figure 64 shows that the motors 2, 4 and 5 had the similar strength of signal with mean values of 1295.56, 1300.84 and 1304.08 respectively which displays the motors 2, 4 and 5 were relatively more stressed.

The pitch graph shown in Figure 66 depicted a similar variation to that of roll graph. The actual pitch variation is from -4.61 to 4.37 with an average of 0.28 while the target pitch varying between -1.92 and 2.65 with an average of 0.35.

The yaw graph shown in Figure 67 depicts the mimimal variation among the three. The actual variation is from 46.59 to 56.4 with an average of 50.4 while the actual yaw varises from -46.59 to 95.89 with an average of 50.45.

The climb rate curve was also plotted as shown in Figure 68 which displays the vertical speed of the drone throughout the flight. The climb rate at take-off is maximum with 82 m/s with the average climb rate being 7.31 m/s. There is an average variation of 1.01 m/s between the actual and desired climb rate.

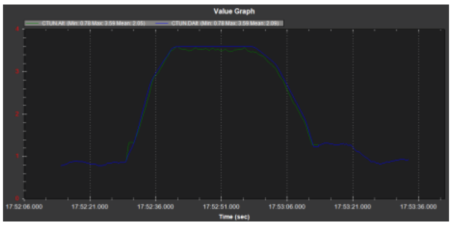

Figure 60: Actual and Desired Altitude vs Time

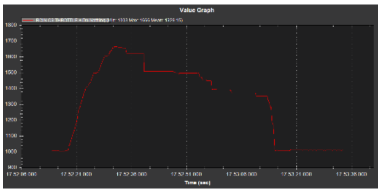

Figure 61: Throttle PPM Signal

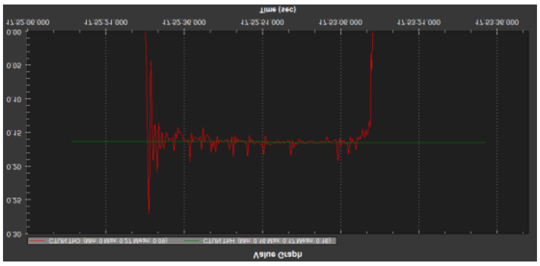

Figure 62: Throttle Output Curve

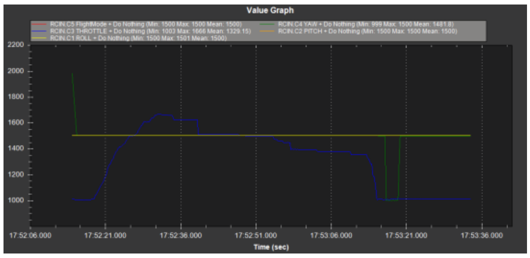

Figure 63: PWM input Signals

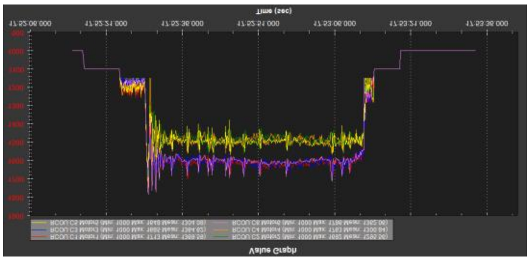

Figure 64: PWM Signals to the Motors

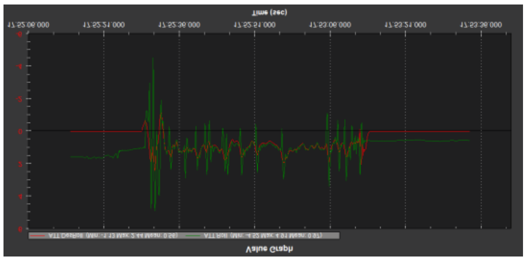

Figure 65: Actual and Desired Roll vs Time

Figure 66: Actual and Desired Pitch vs Time

Figure 67: Actual and Desired Yaw vs Time

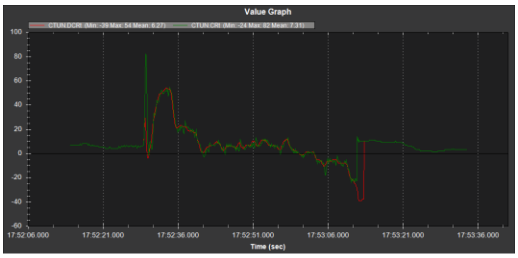

Figure 68: Climb Rate vs Time

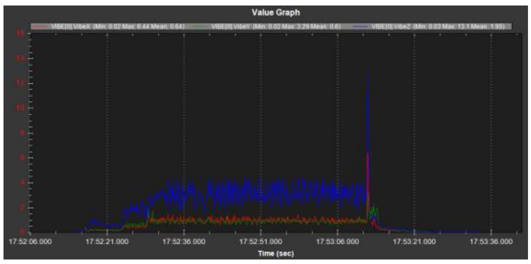

Figure 69: Vibrations in Different Axes

The vibrations present on the drone about all 3-axes of 3D space is plotted as shown in Figure 69. The mean vibration along x ,y and z axes are 0.64 m/s^2, 0.6 m/s^2 and 1.95 m/s^2 respectively which shows minimal vibration along y axis, medium along x and maximum along z axis. The maximum vibration of 13.1 m/s^2 reported along z axis lies under the limit and shows the sound performance of drone during flight. This level of vibration is reported at landing of the drone due to impact.

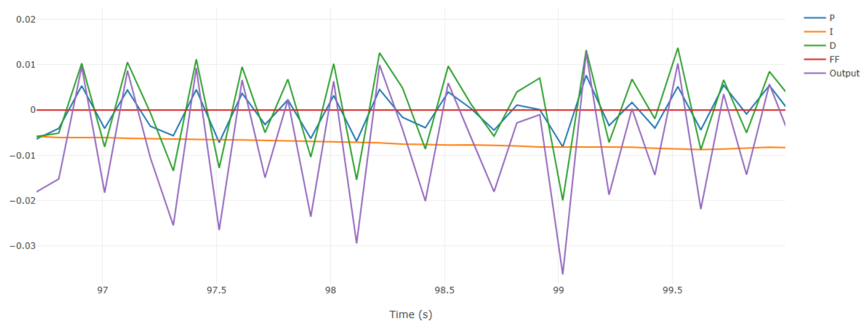

Figure 70: PID Graph with Payload

The PID graph of the flight with 200ml payload is shown in Figure 70. The proportional term, derivative term and output show repeated oscillations with an almost linear integral term. P graph shows rapid oscillation around zero indicating a value high for liquid payload. D graph shows even larger spikes indicating a slow reaction to rapid changes. I graph shows smooth and slightly negative value indicating little accumulated error with the controller compensating the steady state error. The output graph shows much larger variation indicating the response of the combined PID controller and is affected by sloshing liquid.

CHAPTER 5: COST INCURRED

S.N	Particulars	Quantity	Cost Incurred (NRS)
1.	Pixhawk	1	17465
2.	Pixhawk power module	1	1663.89
3.	Anti-vibration shock absorber	1	947.5
4.	One meter pipe	1	517.23
5.	BONKA 4S 25C 13000mAh battery	1	26077.5
6.	11" propeller set +1 extra	4	7550.66
7.	ESC 40A (Readytosky)	9	18744
8.	750 kV motor (FlyCat -5010)	7	20738.4
9.	750 kV motor (Lyla -5010)	2	13160
10.	Diaphragm pump (1-3 L/min) and sprayer	1	1826
11.	Battery Charger and Flysky	1	14610
12.	Aluminium 6061 square tube (20 ft.)	2	2500
13.	Aluminium 6063 plate (3mm)	1	10439
14.	CNC operation base plate	2	6200
15.	Type-B USB cable	2	600
16.	Epoxy and Glue	5	1000
17.	Inch tape, Scissor & Cutter	1	520
18.	Insulation & Double sided tape	5	490
19.	Plier & Screwdriver set	1	720
20.	Analog and digital spring balance	1	300
21.	Plastic pesticide tank and nozzles	4	660
22.	GPS folding stand and module	1	5177.18
23.	PETG 1Kg roll	1	3000
24.	Nut and bolt		1500
25.	15 x 5.5" carbon fiber propeller set	4	12000
26.	Soldering wire and iron	2	1150
27.	Measuring cylinder 100 ml and funnel	1	800
28	Miscellaneous		5000
29.	Total		175206.4

Table 21: Cost Incurred

CHAPTER 6: CONCLUSION

6.1 Conclusion

The design and development of the pesticide-spraying drone was successful with a total payload carrying capacity of 0.5L. The fabricated drone displayed remarkable stability during flight maneuvers and spraying activity. The hexacopter drone experiences a maximum stress of 14.2 MPa under load, maintaining the drone's structural integrity. The spraying system displayed best performance at an altitude range of 1400mm-1600mm with a swath width of 2400mm at static conditions. About 25% of the liquid was lost during spray test and average droplet area was found to be 5.5-12.5mm^2 in five different samples taken. The recorded flight time of the drone with payload is 5 minutes. The analytical thrust calculation of 15-inch prop was 17.23N while the practical and simulated values were 12.9167N and 13.5N thrust. The practical and simulated thrust values were found to be close to each other with 4.32% which lies within acceptable range mentioned by research papers.

6.2 Future Recommendation

The future recommendations from this project are mentioned below:

i. Replace the Aluminium material with a lightweight material like carbon fiber.
ii. Research into autonomy and path planning of the drone.
iii. Design the pesticide-spraying drone for a greater payload.
iv. Economic analysis of the pesticide spraying drone.
v. Integration of electronic components into a single functional chip.

References

Akele, Y. K., & Akele, B. K. (2025). *Generative design and structural optimization of a hexacopter frame for agricultural UAV spraying*. *43*.

Alfonsi, G. (2009). *Navier – Stokes Equations for Turbulence Modeling*. *62*(July). https://doi.org/10.1115/1.3124648

Anken, T., Saravanan, G., Waldburger, T., Werthmüller, J., Wohlhauser, R., & Sanderson, G. (2024). Transversal distribution of a spray drone applying different nozzles and measuring methods. *Crop Protection*, *179*(January), 106603. https://doi.org/10.1016/j.cropro.2024.106603

Butt, M. Z., Nasir, N., Battery, I., Okuyama, K., & Yoshida, N. (n.d.). *Application of Drone Systems for Spraying Pesticides in Advanced Agriculture : A Review Application of Drone Systems for Spraying Pesticides in Advanced Agriculture : A Review*. https://doi.org/10.1088/1757-899X/1259/1/012015

D., Y. (2015). *Development and evaluation of drone mounted sprayer for pesticide applications to crops*.

Dutta, G., & Goswami, P. (2020). *Application of drone in agriculture : A review Gopal Dutta and Purba Goswami*. *8*(5), 181–187.

Fejes, J. (2024). *Numerical Analysis of a Rotating Propeller*.

Fogelberg, J. (n.d.). *Navigation and Autonomous Control of a Hexacopter in Indoor Environments*.

Gurugubelli, S., Kaveri, G., Krishna, K. V., & Manideep, G. (2023). *Polymer & Composites Optimal Design and Fabrication of Drone for Agricultural Purpose*. *11*(12), 81–93.

Gutierrez-rivera, M. E., Rumbo-morales, J. Y., Ortiz-torres, G., Gascon-avalos, J. J., Sorcia-vázquez, F. D. J., Torres-cantero, C. A., Buenabad-arias, H. M., Guillen-escamilla, I., López-osorio, M. A., Zurita-gil, M. A., Calixto-rodriguez, M., Rosales, A. M., & Juárez, M. A. (2024). *Design , Construction and Finite Element Analysis of a Hexacopter for Precision Agriculture Applications*. 1239–1267.

Ibrahim, N. (2017). *DESIGING A REAL MATHEMATICAL MODEL OF A*

HEXACOPTER IN THE INERTIAL FRAME. *73*(045), 91–94.

Javier, C., Perdomo, L., Orquera, M., Millet, D., & Gabriel, B. (2025). Influence of inertia relief analysis on the topological optimisation of unconstrained structures. *International Journal on Interactive Design and Manufacturing (IJIDeM)*, *19*(6), 4395–4415. https://doi.org/10.1007/s12008-024-02021-8

Karki, R., & Dangol, K. (2023). *Pesticide Use and Health Effects among Nepalese Farmers : A Cross - Sectional Study in Tokha Municipality*. https://doi.org/10.4103/ijoem.ijoem

Kavya, T., & Shirwal, S. (2024). *Influence of Spray Parameters of a UAV Sprayer on Droplet Size in Paddy Spraying*. *30*(11), 749–761.

King, A. (n.d.). *THE FUTURE OF AGRICULTURE*.

Magnussen, Ø., Ottestad, M., & Hovland, G. (2015). Multicopter design optimization and validation. *Modeling, Identification and Control*, *36*(2), 67–79. https://doi.org/10.4173/mic.2015.2.1

Mahir, A. A., & Ozan, A. Y. (2026). *Numerical investigation of propeller flow field using mrf model*. *28*(1), 435–448. https://doi.org/10.25092/baunfbed.

Mitchell, J. W. (n.d.). *No Title*.

Moussid, M. (2015). *Dynamic Modeling and Control of a HexaRotor using Linear and Nonlinear Methods*. *9*(5), 9–17.

Nepal Rastra Bank Current Macroeconomic and Financial Situation of Nepal. (2025). *July*, 1–12.

Oktay, T., Eraslan, Y., & Program, O. (2020). *COMPUTATIONAL FLUID DYNAMICS (CFD) INVESTIGATION OF A QUADROTOR UAV PROPELLER*. *June*, 5–7.

Optimization, P., Structural, O. F., Design, F., High, F. O. R., & Hexacopter, P. (2024). *Black Sea Journal of Engineering and Science PARAMETRIC OPTIMIZATION OF STRUCTURAL FRAME DESIGN*. 854–865. https://doi.org/10.34248/bsengineering.1499762

Paudel, M. N. (2016). *Prospects and limitations of agriculture industrialization in Nepal*. *4*, 38–63.

Rizon, M., Ang, C. K., Solihin, M. I., Razlan, Z. M., Desa, H., Bakar, S. A., Khairunizam, W., & Ibrahim, Z. (2020). *Effects of Variable Arm Length on UAV Control Systems*. *7*, 91–97.

S, L. G. G., Varunkumar, J. M., Ghorpade, E. A., Rushab, B., & Vijayakumar, M. N. (2021). *Review on Design and Development of Quadcopter for Smart Agriculture*. *July*, 3681–3685.

Saleh, T., & Aboukassem, K. (2018). *Study the Equations of Motion for a Hexacopter Aerial Vehicle based on The Newton-Euler Method*. *6*(4), 17–22.

Sambaiah, A., Madhuri, C., Rao, K. P. C., Kamakshi, N., & Lakshmi, N. V. (2023). *Performance Evaluation of Hexacopter UAV (ANGRAU-PUSHPAK) Spraying for Management of Chilli Aphids , Myzus Persicae (Sulz .)*. *70*(4), 508–518.

Sanca, A. S., Laura, T. L., Cerqueira, J. F., & Alsina, P. J. (2010). *XVIII Congresso Brasileiro de Automática / 12 a 16-setembro-2010, Bonito-MS*. 1454–1461.

Sapkota, M. (2023). *Nepalese Journal of Development and A Peer-Reviewed , Open Access Journal , Index in NepJOL Issues and Challenges of Modernization in Nepal : A Development Perspective*. *20*(1).

Saric, I., Masic, A., & B, M. D. (2021). *Hexacopter Design and Analysis*. *1*, 74–81.

Shahi, B. B. (2022). *Agricultural Modernization and Rural Development : Reference to Traditional Agriculture Transformation in Nepal*. 46–56.

Shaw, K. K., & Vimalkumar, R. (2021). *Design and Development of a Drone for Spraying Pesticides , Fertilizers and Disinfectants*. *9*(05), 1181–1185.

Talaeizadeh, A., Sharifi, I., Alasty, A., & Ghatrehsamani, S. (2025). Smart Agricultural Technology Agricultural spraying drones : A comprehensive review. *Smart Agricultural Technology*, *12*(October), 101519. https://doi.org/10.1016/j.atech.2025.101519

Yogi, L. N., Thalal, T., & Bhandari, S. (2025). Heliyon The role of agriculture in Nepal ' s economic development : Challenges , opportunities , and pathways for modernization. *Heliyon*, *11*(2), e41860. https://doi.org/10.1016/j.heliyon.2025.e41860

Zhang, H., Wen, S., Chen, C., Liu, Q., Xu, T., Chen, S., & Lan, Y. (2023). *Downwash airflow field distribution characteristics and their effect on the spray field distribution of the DJI T30 six-rotor plant protection UAV*. *16*(2), 10–22. https://doi.org/10.25165/j.ijabe.20231602.8094

https://www.flyeye.io/wp-content/uploads/2025/09/Multirotor-drones-quadcopters-hexacopters-octocopters-1028x685-1-e1759262310336.webp

APPENDIX

Figure 71: Mission Planner Interface

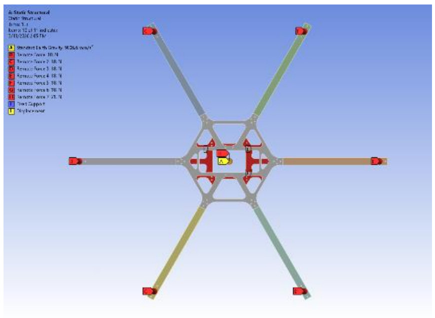

Figure 72: Boundary Conditions Imposed on the Final Design

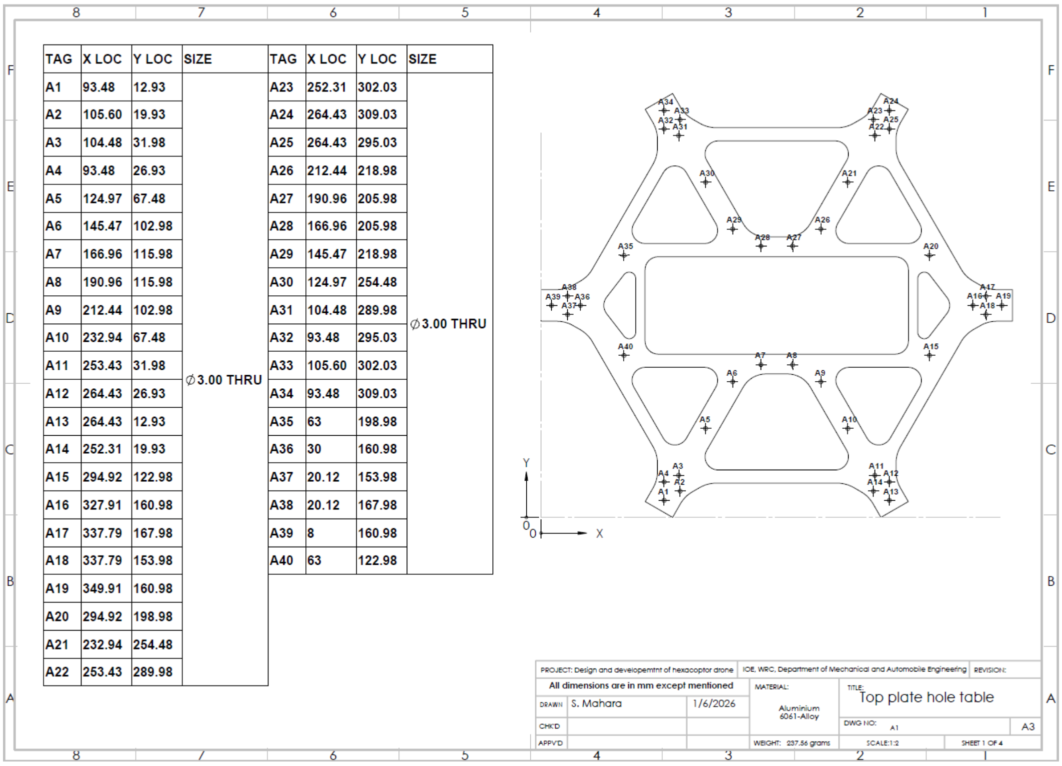

TAG	X LOC	Y LOC	SIZE
A1	93.48	12.93	∅3.00 THRU
A2	105.60	19.93	
A3	104.48	31.98	
A4	93.48	26.93	
A5	124.97	67.48	
A6	145.47	102.98	
A7	166.96	115.98	
A8	190.96	115.98	
A9	212.44	102.98	
A10	232.94	67.48	
A11	253.43	31.98	
A12	264.43	26.93	
A13	264.43	12.93	
A14	252.31	19.93	
A15	294.92	122.98	
A16	327.91	160.98	
A17	337.79	167.98	
A18	337.79	153.98	
A19	349.91	160.98	
A20	294.92	198.98	
A21	232.94	254.48	
A22	253.43	289.98	

TAG	X LOC	Y LOC	SIZE
A23	252.31	302.03	∅3.00 THRU
A24	264.43	309.03	
A25	264.43	295.03	
A26	212.44	218.98	
A27	190.96	205.98	
A28	166.96	205.98	
A29	145.47	218.98	
A30	124.97	254.48	
A31	104.48	289.98	
A32	93.48	295.03	
A33	105.60	302.03	
A34	93.48	309.03	
A35	63	198.98	
A36	30	160.98	
A37	20.12	153.98	
A38	20.12	167.98	
A39	8	160.98	
A40	63	122.98	

Figure 73: Upper Plate Drawing for CNC Machining

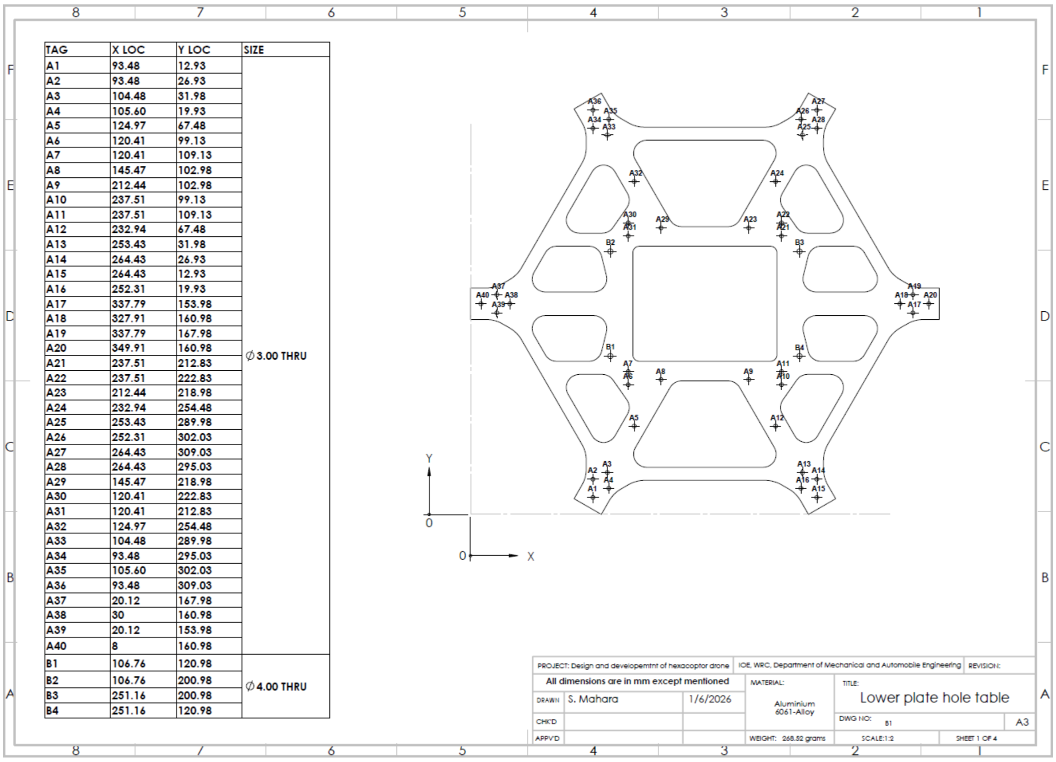

TAG	X LOC	Y LOC	SIZE
A1	93.48	12.93	∅3.00 THRU
A2	93.48	26.93	
A3	104.48	31.98	
A4	105.60	19.93	
A5	124.97	67.48	
A6	120.41	99.13	
A7	120.41	109.13	
A8	145.47	102.98	
A9	212.44	102.98	
A10	237.51	99.13	
A11	237.51	109.13	
A12	232.94	67.48	
A13	253.43	31.98	
A14	264.43	26.93	
A15	264.43	12.93	
A16	252.31	19.93	
A17	337.79	153.98	
A18	327.91	160.98	
A19	337.79	167.98	
A20	349.91	160.98	
A21	237.51	212.83	
A22	237.51	222.83	
A23	212.44	218.98	
A24	232.94	254.48	
A25	253.43	289.98	
A26	252.31	302.03	
A27	264.43	309.03	
A28	264.43	295.03	
A29	145.47	218.98	
A30	120.41	222.83	
A31	120.41	212.83	
A32	124.97	254.48	
A33	104.48	289.98	
A34	93.48	295.03	
A35	105.60	302.03	
A36	93.48	309.03	
A37	20.12	167.98	
A38	30	160.98	
A39	20.12	153.98	
A40	8	160.98	
B1	106.76	120.98	∅4.00 THRU
B2	106.76	200.98	
B3	251.16	200.98	
B4	251.16	120.98	

Figure 74: Base Plate Drawing for CNC Machining

Figure 75: PID Tuning Apparatus

Figure 76: Thrust test apparatus of the Propeller

Figure 77: Patternator Test for Spray Uniformity

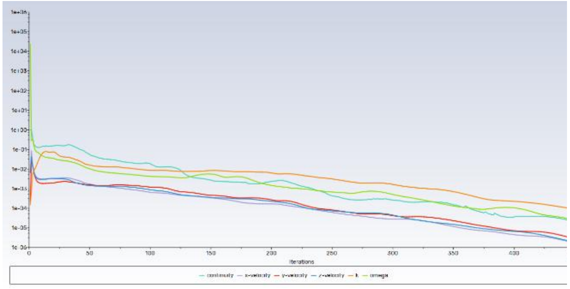

Figure 78: Residual Convergence Graph

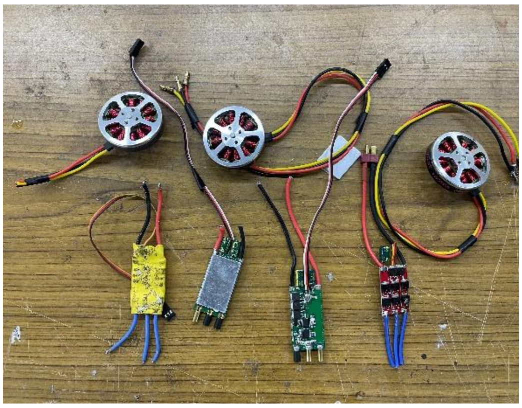

Figure 79: Faulty Components

Figure 80: Droplet Test

Figure 81:Members Fabricating Drone Frame